Thesis for the degree of Doctor of Philosophy

Modelling of Multicomponent Fuel Sprays

VIGNESH PANDIAN MUTHURAMALINGAM

Department of Mechanics and Maritime Sciences
CHALMERS UNIVERSITY OF TECHNOLOGY
Göteborg, Sweden 2021

Modelling of Multicomponent Fuel Sprays
VIGNESH PANDIAN MUTHURAMALINGAM
ISBN 978-91-7905-431-1

Doktorsavhandlingar vid Chalmers tekniska högskola
Ny serie nr 4898
ISSN 0346-718X

Department of Mechanics and Maritime Sciences
Chalmers University of Technology
SE–412 96 Göteborg, Sweden
Telephone + 46 (0) 31 – 772 1000

Cover: Fuel-air mixing at diesel engine conditions, arrows represent vectors of gas velocity.

Typeset by the author using LaTeX.

Printed by Chalmers Reproservice
Göteborg, Sweden 2021

to curiosity

Modelling of Multicomponent Fuel Sprays
VIGNESH PANDIAN MUTHURAMALINGAM
Department of Mechanics and Maritime Sciences
Chalmers University of Technology

Abstract

The use of fuel blends (conventional fuels blended with renewable ones) has gained importance in the automotive industry as an option to reduce emissions and dependence on fossil fuels. In order to make the fuel blends commercially viable, computational fluid dynamics (CFD) is used to complement the experiments (done on engines or spray chambers) by providing fundamental insight into spray formation. The work presented in this thesis is focused on modelling and CFD simulation of multicomponent fuel sprays.

The spray model used in this work is the stochastic blob and bubble model (VSB2) which is a discrete multicomponent fuel spray model. One of the strengths of the model is that it uses thermodynamic equilibrium to calculate heat and mass transfer to ensure that there is no over- or under-estimation of the temperature or evaporated mass. The VSB2 also uses minimal tuning parameters for modelling. The present work extended the spray model to handle multicomponent fuels. One of the main challenges in modelling multicomponent fuels is to handle differential evaporation correctly. To address this, a non-linear equation solver was implemented . The solver interfaces with the OpenFOAM code containing the spray model. One of the main benefits of the newly implemented solver is that it can be scaled to handle a large number of fuel components with minimal effort.

The multicomponent fuel spray model was validated with experimental data for one, two and three fuel components respectively in three separate cases and showed reasonably good agreement. Apart from this, the model was used to study the influence of non-ideal vapor liquid equilibrium (VLE) and showed that it is important to consider non-ideal VLE for fuels with polar molecules. The model was also used to study the influence of resolving the injector orifice and the counterbore of a gasoline direct engine (GDI) injector in two separate studies. The results of all the studies can be found in the appended manuscripts.

Having thus established the multicomponent fuel spray model in through this work, in future, it can be combined with detailed chemical mechanisms and combustion models to extend the studies to investigate combustion of multicomponent fuels.

Keywords: CFD, multicomponent fuel sprays, differential evaporation, stochastic blob and bubble model, secondary breakup, diesel and gasoline engine conditions, resolving injector orifice, GDI injector, resolving counterbore

Acknowledgments

My thesis would not be complete without acknowledging the important people involved during the course of my work. First of all I thank my supervisor Adjunct Prof. Anders Karlsson for his guidance throughout the project. Thanks for the long discussions on the VSB2 model. Your experience and insight provided an important support in my PhD.

I thank Prof. Ingemar Denbratt for giving me the opportunity to work on this project. I also thank him for his continuous support throughout the project till the very end.

I thank my co-supervisor Prof. Michael Oevermann for the additional academic support in my project when asked for. I thank the members of CERC working group for their feedback during the quarterly meetings. I acknowledge CERC for funding the project.

A special thanks to my office mates, also my buddies, Andreas Nygren and Michael Saccullo for all the good times we had both at and outside work, and for all the work related and non-work related discussions. It was a privilege to share office with you guys all the way till the end.

PhD is not all just about working. I have to definitely thank all the colleagues at CaPS for the wonderful lunch breaks, fika breaks and after works. You made my stay at CaPS memorable. Thanks to Jelmer, Zhiqin, Akichika, Magnus, Sreelekha, Mindaugas, Marco, Amirreza, Chengjun and Tankai for the fun times at CaPS. But the list is not limited and my acknowledgment goes out to everyone involved in one way or the other during my time at CaPS. I have to also thank Timothy for the interesting discussions and also for the short time I spent with him at the Trämuseum , learning to maintain steam engines. I thank Patrik for all the long and informative discussions, Joop for the discussions on Powertrain Mechanics and training, Jan Eismark for short period we collaborated at work and for the opportunity to ride along on his classic sail boat.

Thanks to Elenor for all the bill related questions and patiently listening to my Swinglish. And I thank Karin as well for patiently listening to my Swinglish. I thank Blagica for all the administrative support.

I have to acknowledge the running club solvikingarna for literally keeping me up and running during the dark, cold winter days and preparing me for competitions.

Finally I have to thank my parents and my brother for understanding and supporting me through both good and tough times. I thank my parents for the support they have given to me to follow my plans.

VIGNESH PANDIAN MUTHURAMALINGAM
Göteborg, January 2021

List of Publications

This thesis is based on the following appended papers:

Paper I. Vignesh Pandian Muthuramalingam and Anders Karlsson. *Development and validation of a multicomponent fuel spray model (VSB2 model).* in SAE International Powertrains Fuels and Lubricants Meeting Beijing, (2017).

Paper II. Vignesh Pandian Muthuramalingam and Anders Karlsson. *Influence of Considering Non-Ideal Thermodynamics on Droplet Evaporation and Spray Formation (for Gasoline Direct Injection Engine Conditions) Using VSB2 Spray Model.* in SAE WCX Detroit, (2018).

Paper III. Vignesh Pandian Muthuramalingam, Andreas Nygren and Anders Karlsson. *A comprehensive study on the influence of resolving an injector orifice and the influence of creating stripped off droplets on spray formation using the VSB2 spray model.* accepted in Atomization and Sprays, (2020).

Paper IV. Vignesh Pandian Muthuramalingam and Anders Karlsson. *Validation of a multicomponent fuel spray model for gasoline direct engine conditions (ECN spray G) and study on the influence of resolving the counter-bore injector.* submitted to SAE International Journal of Fuels and Lubricants, (2020).

List of Acronyms

ASME	–	American society of mechanical engineers
ASOI	–	After start of injection
CDF	–	Cumulative distribution function
CFD	–	Computational Fluid Dynamics
DNS	–	Direct numerical simulation
ECN	–	Engine Combustion Network
GCI	–	Grid convergence index
GDB	–	Gasoline diesel blend
GDI	–	Gasoline direct injection
HD	–	Heavy-duty
ICE	–	Internal combustion engine
KH	–	Kelvin-Helmholtz
LES	–	Large eddy simulation
LPT	–	Lagrangian particle tracking
NDF	–	Number density function
NRTL	–	Non-random two liquid
OpenFOAM	–	Open-source field operation and manipulation
PBE	–	Population balance equation
PISO	–	Pressure implicit with splitting operators
QBMM	–	Quadrature-based moment method
RANS	–	Reynolds-averaged Navier-Stokes
RE	–	Richardson extrapolation
RT	–	Rayleigh-Taylor
SDS	–	Sustainable development scenario
SMD	–	Sauter mean diameter
SUNDIALS	–	Suite of Nonlinear and differential/algebraic equation solvers
TAB	–	Taylor analogy breakup
VLE	–	Vapor liquid equilibrium
VOF	–	Volume of fluid
VSB2	–	Stochastic Blob and Bubble

List of Roman symbols

A	–	Area of cross section of injector orifice $[m^2]$
C_D	–	Discharge coefficient of nozzle [-]
D_{blob}	–	Diameter of blob before secondary breakup [m]
D'_{blob}	–	Blob diameter after secondary breakup [m]
D_{bub}	–	Diameter of bubble [m]
D_e	–	Effective diameter of droplets in a blob [m]
D_j	–	Diffusion coefficient for fuel component j $[\frac{m^2}{s}]$
D_s	–	Stable droplet diameter [m]
D_{sn}	–	Normalized stable blob diameter [-]
dt_s	–	Sub time step [s]
f	–	correction factor that accounts for influence of heat transfer on mass transfer coefficient [-]
h	–	Specific enthalpy of gas $[\frac{J}{kg}]$
$h_{fuel,vap,i}$	–	Gas phase specific enthalpy of fuel component i $[\frac{J}{kg}]$
k	–	Turbulent kinetic energy of gas $[\frac{m^2}{s^2}]$
Kn	–	Knudsen number [-]
l_{diff}	–	Turbulent length scale based on turbulent diffusion [m]
$M_{fu,i}$	–	Molecular weight of the gaseous fuel component i $[\frac{kg}{mol}]$
M_{mix}	–	Molecular weight of the gas mixture $[\frac{kg}{mol}]$
M_{sn}	–	Normalized stripped off mass [-]
$m_{evap,ij}$	–	Evaporated mass for mass package i and fuel component j [kg]
m_{eq}	–	Mass that is left behind in a blob after evaporation [kg]
m	–	Mass of gas in a computational grid cell [kg]
m_{blob}	–	Mass of a blob [kg]
$m_{blob,i,j}$	–	Mass of a blob in mass package i and fuel component j [kg]
m_s	–	Liquid mass stripped off from parent blob due to secondary breakup [kg]
N_f	–	No of fuel components in the multicomponent fuel mixture [-]
N_{rep}	–	Representative number of droplets in a blob [-]
Nu	–	Nusslet number [-]
Oh	–	Ohnesorge number [-]
P_{gas}	–	Gas pressure $[\frac{kg}{ms^2}]$
$P_{i,v}$	–	Vapor pressure of fuel component i $[\frac{kg}{ms^2}]$
$P_{sat,i}$	–	Saturation pressure for fuel component i $[\frac{kg}{ms^2}]$
S	–	Strain rate tensor $[\frac{1}{s^2}]$
$\dot{S}_M$	–	Evaporation source term from spray model [kg]
$\dot{S}_I$	–	Momentum source term from spray model $[\frac{kgm}{s}]$

$\dot{S}_E$	–	Enthalpy source term from spray model $[J]$
Sh	–	Sherwood number [-]
T_{blob}	–	Liquid temperature of the blob [K]
T_{eq}	–	Equilibrium temperature of remaining blob after evaporation [K]
T_f	–	Film temperature [K]
We_{cr}	–	Critical weber number [-]
$X_{i,l}$	–	Mole fraction of fuel component i in the liquid droplet [-]
$Y_{fu,eq,i}$	–	Equilibrium mass fraction of fuel component i [-]
$Y_{fu,sat,i}$	–	Saturated fuel mass fraction for fuel component i [-]

List of Greek symbols

α	–	Volume fraction of the dispersed phase [-]
α_l	–	Laminar thermal diffusivity $[\frac{kg}{ms}]$
α_t	–	Turbulent thermal diffusivity $[\frac{kg}{ms}]$
γ	–	Activity coefficient [-]
$\Delta h_{vap,i}$	–	Enthalpy of vaporization of fuel component i $[\frac{J}{kg}]$
Δm_i	–	mass of fuel component i evaporated until saturation [kg]
Δt	–	Computational time step [s]
ϵ	–	Rate of dissipation of the turbulent energy of gas $[\frac{m^2}{s^3}]$
θ	–	Gas phase correction factor [-]
λ	–	Thermal conductivity of the liquid film $[\frac{W}{mK}]$
λ_m	–	Molecular mean free path length [m]
μ	–	Laminar viscosity of gas $[\frac{kg}{ms}]$
μ_t	–	Turbulent viscosity of gas $[\frac{kg}{ms}]$
ξ	–	Internal coordinate vector of the dispersed particle [-]
σ	–	Variance of Gaussian distribution [-]
$\tau_{breakup}$	–	Secondary breakup time constant [s]
$\tau_{m,ij}$	–	Evaporation time constant for mass package i and fuel component j [s]
$\tau_{T,i}$	–	Heat transfer time constant for mass package i [s]
ϕ	–	Vector property [-]

Contents

Part I

Introductory chapters

Chapter 1

Introduction

1.1 Background

Transportation is fundamental to modern societies, and a growing global economy implies an increasing need to transport goods and people both within and across borders. This in turn implies increasing energy consumption which is compounded by population growth. Some of the by-products produced of the energy conversion processes currently used to power vehicles are emitted substances known to be harmful. In particular, the combustion of conventional fossil fuels continues to be the main source of power for transportation but emits both greenhouse gases and atmospheric pollutants harmful to the environment and human health. While electric cars are becoming increasingly common, heavy duty vehicles remain dependent on internal combustion engines (ICEs) burning fossil fuels for want of a viable alternative energy source. Additionally, it is not currently viable to electrify ships or aircraft. The aviation industry thus remains reliant on kerosene, and its emissions have increased by 2 % annually on average since 2000 [22]. International shipping accounted for 2 %of global energy related CO_2 emissions in 2019 [24], while tailpipe emissions from heavy-duty (HD) vehicles have increased by an average of 2.6 % annually on average since 2000. Trucks accounted for over 80 % of these emissions. Overall, transportation is currently responsible for 24 % of all direct CO_2 emissions from fuel combustion [25]. While these numbers are not good, there have been improvements, and efforts to reduce emissions continue. The sustainable development scenario (SDS) based on the Paris climate agreement aims to prevent global temperatures from rising by more than 2 ^{o}C until the end of the century. Figure 1.1 shows how global emissions due to trucks are forecast to change over time. From 2018, when the SDS came into effect, emissions are projected to rise briefly before stabilizing and then falling. And overall global CO_2 emissions from the energy sector and industrial processes are projected to drop from 35.8 billion tonnes in 2019 to less than 10 billion tonnes in 2050 according to the SDS plan which relies in part on increasing electrification and the use of alternative fuels. Efforts are also being made to make combustion cleaner and more efficient. The use of biofuels and blends of conventional and renewable fuels (e.g. biodiesel) for electricity generation is increasing (Figure 1.2), and such blended fuels have also attracted interest in the automotive industry because of their potential

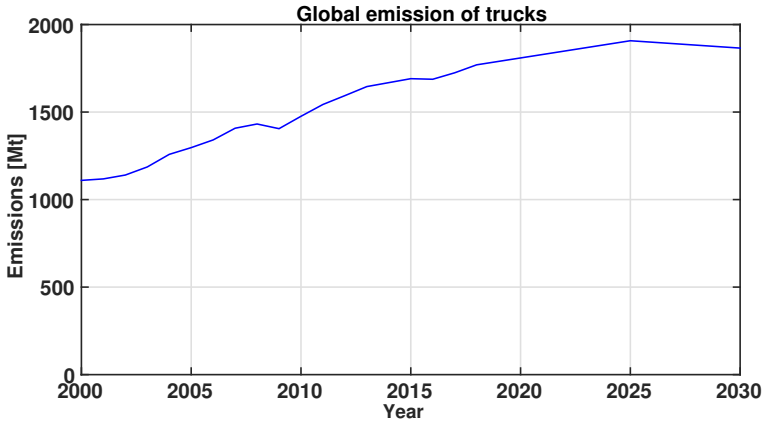

Figure 1.1: Changes in global emissions due to trucks over time. Source of Data: [23].

to reduce net emissions. Considerable research and development effort has been

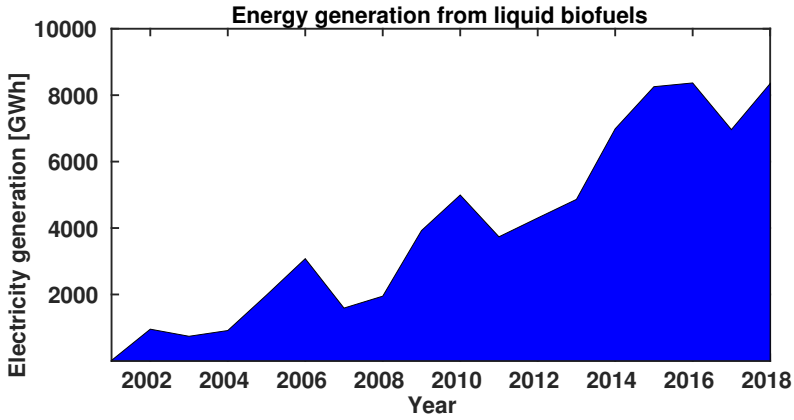

Figure 1.2: Changes in electricity generation from liquid biofuels over time. Source of data: [21].

invested into clean fuels and clean combustion strategies for Internal Combustion Engines.

1.2 Role of Computational Fluid Dynamics (CFD) in developing cleaner engines

Efforts to make clean fuels and combustion strategies commercially viable rely on laboratory experiments done using engines or under engine-like conditions. CFD is frequently used to complement such experimental tests. CFD models fluid flows, heat transfer and chemical reactions in specific engine geometries, engine subsystems, or simplified systems mimicking engine conditions. It does this by solving conservation equations and using models to describe physical processes (e.g. evaporation, heat transfer, combustion). CFD models must be validated against experimental data

but are less expensive to perform than experiments and are therefore increasingly used to study fundamental phenomena and optimize designs. Designs optimized by CFD can then be tested experimentally. There are ongoing efforts to improve the models used in CFD to increase the accuracy of the predictions and also reduce the tuning of models to make them predictive.

Experiments are done on engines at different load points to study processes such as gas exchange, fuel injection, fuel-air mixing, combustion, work output, and emissions. Alternatively, experiments can be done using simplified set-ups such as a constant volume combustion chamber (using the same operating conditions as in the engine). Such scaled down experiments are typically performed to study processes such as injection and the formation and combustion of fuel sprays. Their results can then be clarified by performing CFD simulations to explain the observed spray behavior.

Focus of this thesis The work presented here focuses on the modelling and CFD simulation of multicomponent fuel sprays and validation of the resulting models against experimental data generated using constant volume combustion chambers under non-combusting conditions. Particular emphasis is placed on understanding the physical processes involved in spray formation, especially secondary breakup, the evaporation of multicomponent fuels, and spray-gas interaction

1.3 Motivation

This section summarizes previous studies on three key topics and the knowledge gap which motivated this project. The topics addressed are modelling of multicomponent fuels, resolving the fuel injector orifice in CFD simulations, and non-ideal Vapor Liquid Equilibrium (VLE).

Modelling of multicomponent fuels The spray model used in this work was originally developed to describe single component fuels. It was tested and validated against experimental data, achieving good agreement for the tested operating conditions [38]. This work presents efforts to extend the model to handle multicomponent fuel sprays. The properties of each individual fuel component must be considered when modeling the physical processes affecting spray behavior (e.g. heat transfer and evaporation). The treatment of preferential evaporation is particularly challenging because each component evaporates at its own rate, and the evaporation of one component will in turn affect that of all the others. The equations describing these evaporation processes are thus coupled and in addition they are also non-linear. In this work the goal was to implement an efficient method for solving differential evaporation for multicomponent fuels that can be scaled with minimal effort to handle a large number of fuel components.

Resolving fuel injector orifice Sufficiently fine grid cells are required to ensure accurate resolution of velocity and mixing gradients. The question of what grid

size is sufficient has therefore often been discussed in the spray literature. Kösters [38] concluded that a grid size of the order of the orifice diameter is required for reasonable predictions. Seneccal [63] performed a comprehensive grid study using Adaptive Mesh Refinement (AMR) for a wider range of grid sizes which provides a good insight into grid sensitivity and a good argument for what is sufficient grid size. Some more examples on grid sensitivity are [69], [1], [48], [41], [4]. [69] performed grid sensitivity studies for diesel engine conditions and used the unsteady jet-model of [1] to mimimize grid dependence. [41] concluded that grid sizes particularly influence the liquid phase predictions (e.g. liquid length). The use of Adaptive Mesh Refinement (AMR) as a tool for simulating high-pressure diesel sprays was also highlighted in the same work. Grid sensitivity study was also performed in [16] and a method for reducing grid dependency by limiting the turbulent length length scale in the core of the spray was presented. This method is also used in the current work performed by the author. Apart from considering grid resolution in the near orifice region, it has been shown that it is important to resolve the injector orifice itself. Abraham [2] performed simulations with resolved injector orifice and suggested that at least 2 cells across the orifice are needed to accurately predict gas jets. In the study performed by [63], mentioned earlier, the influence of resolving grid cells smaller than orifice diameter was studied for sprays but focussed mainly only on liquid and vapor penetration values.

To date, few studies have examined in detail, the influence of injector orifice resolution on the predicted behavior of fuel sprays under high pressure and temperature diesel engine-like conditions. The influence of injector orifice resolution on predicted spray formation was therefore investigated in this work. In addition, the influence of resolving a counterbore Gasoline Direct Injection (GDI) injector was also studied. Experiments have been done studying the influence of using counterbore GDI injectors with respect to fuel-air mixing, fuel efficiency and emissions e.g. [47], [34]. In [47] it was shown that the counterbore injector had better air-entrainment, longer spray penetration, lower fuel consumption and emissions over the standard injector, even if the differences were small. There have also been works done on the simulations of GDI injectors e.g. [34], [66], [60]. These works provided insight into the nozzle and near nozzle flow and primary atomization. Full spray RANS simulations were also done on Spray-G conditions for three component surrogate fuel by different modelling groups and presented in ECN 7 workshop [14]. They provided valuable insight but the counterbore was not resolved in these studies. Few studies to date have focussed on the influence of resolving counterbore on full spray RANS simulations. It was therefore the motivation in the current work to take up this study.

Non-ideal VLE Most spray simulations assume ideal thermodynamic behavior when modeling fuel evaporation. This assumption neglects the role of intermolecular forces. However, previous studies [6], [27], [73] have demonstrated that non-ideal thermodynamic behavior must be considered when simulating multicomponent fuels because interactions between different kinds of molecules lead to deviations from

ideal behavior. In this work the influence of considering non-ideal thermodynamics on spray formation is studied.

1.4 Research questions

An important objective in this project was to develop a solver for the coupled non-linear equations governing the evaporation of multicomponent fuels. The solver should interface easily with the existing spray code and should be designed to handle an increasing number of fuel components as required. Having thus extended the spray model to handle multicomponent fuels, the following research questions were sought out to be answered:

- What is the influence of considering non-ideal Vapor Liquid Equilibrium on the differential evaporation of multicomponent fuels? How does the evaporation rate, fuel vapor distribution compare to when assuming ideal VLE?
- What is the influence of resolving the injector orifice on spray predictions (diesel engine conditions) with respect to secondary breakup and evaporation of droplets and what is the influence on the predictions of turbulent kinetic energy and dissipation rate? How can a sufficient orifice resolution be justified?
- In a Lagrangian parcel having a size distribution of droplets, is it justifiable to assign the parcel velocity to all the size distributions? How does this assumption affect the momentum transfer and evaporation of the droplets under diesel engine conditions?
- What is the influence of resolving the counterbore of a GDI injector on spray formation with respect to evaporation of droplets, multicomponent vapor distribution and fuel-air mixing?

1.5 Organization of the thesis

This thesis is organized into 5 Chapters. The current chapter introduces the background factors and research questions that motivated this PhD work. The following chapter provides discussion on the fundamentals of multiphase flows in general and sprays in specific, introducing key concepts used in the rest of the thesis. The third chapter builds on this material and presents a more detailed discussion of the spray model used in this work and it's associated equations. The fourth Chapter discusses model settings, solution algorithm used and summarizes the key results from Papers I-IV on which this thesis work is based. The final Chapter concludes the thesis and presents some interesting avenues for future work. The papers on which this thesis work is based are appended at the end.

Chapter 2

Spray fundamentals

This chapter introduces fundamental concepts that are used and elaborated upon in the subsequent chapter discussing the research methodology. Sprays have varied applications in fields including transportation (in ICEs and gas turbines), manufacturing (e.g. in spray paints), food production (e.g. for coating with flavors and additives), the paper industry (e.g. for coating paper), agriculture (e.g. spraying of insecticides and pesticides), and pharmaceuticals (e.g. in the form of aerosol sprays for nasal administration). A deeper understanding of spray formation and behavior is therefore important for efforts to improve efficiency in these areas. In this work the focus is on sprays for automotive ICE applications.

2.1 Sprays in engines

The automotive industry faces increasingly stringent demands to increase the efficiency of engines while reducing their emissions. A deep understanding of fuel spray formation and its interaction with turbulent air is essential for this purpose. The cleanliness and efficiency of the combustion process in a direct injection engine depends strongly on the characteristics of the fuel spray. It is important for fuel sprays to consist of relatively small droplets that evaporate quickly and mix well with the surrounding air. To ensure that this requirement is fulfilled, one must understand the physical processes governing spray formation, which include droplet breakup, evaporation, heat, momentum and mass transfer, and spray-turbulence interaction. There is considerable interest in replacing conventional fossil fuels with blended fuels containing both conventional fuels and renewable ones to reduce emissions and fossil fuel dependence. This will require a better understanding of multicomponent fuel sprays, and particularly processes such as differential evaporation. Fuel spray models are used to understand spray behavior and complement experimental efforts. A large part of the work presented in this thesis relates to modelling multicomponent fuel sprays, using these models in CFD simulations to predict multicomponent spray behavior, and validating the developed models by comparing the output of the simulations to experimental data.

The remainder of the current chapter introduces some key physical process involved in spray formation, with particular focus on fuel sprays for automotive engine applications.

2.2 Modelling two phase flows

Multiphase flows can be two-phase, three-phase or more than three phase. Here the discussion is limited to two-phase flows although the concepts discussed here can be extended to more phases. Two phase flows can further be classified into gas-liquid, gas-solid and liquid-solid. The following discussion is focussed on gas-liquid flows.

The dispersed and the continuous phases Fuel sprays are multiphase flows consisting of continuous and dispersed phases: the liquid droplets (the dispersed phase) are dispersed in the surrounding gas (the continuous phase). The gas phase can be treated as a continuous phase if Knudsen number of the multiphase system is below 1. The Knudsen number is defined as

$$Kn = \frac{\lambda_m}{L} \tag{2.1}$$

where λ_m is the molecular mean free path length and L is the characteristic physical length scale of the problem of interest. The mean free path length for the gas mixture at the temperatures and pressures relevant to the problem under study (pre-combustion conditions in an automotive engine) is on the order of nanometres. A commonly used characteristic length scale for the mean flow in spray simulations is the nozzle diameter, which is on the order of a few millimetres or hundreds of micrometres. The Knudsen number for such mixtures is thus significantly less than 1, justifying the treatment of the gas as a continuous phase.

Interaction between the phases A multiphase flow can be dense or dilute depending on the volume fraction of the dispersed particles. Multiphase models have to address the interactions between the two phases. A dilute flow can have 1-way or 2-way coupling between the dispersed and the continuous phases. 1-way coupling is when the continuous phase interacts with the dispersed (e.g. Turbulence causing droplet dispersion in fuel sprays). 2-way coupling is 1-way plus the interaction of the dispersed phase with the continuous (e.g. mass, momentum, and energy transfer from the liquid to gas in fuel sprays). Dense sprays can also have interaction between the particles in addition to the previously mentioned interactions. This would then constitute a 3-way coupling (e.g. collision between droplets in sprays) and additionally the dispersed particles can also interact with the wall and this would comprise a 4–way coupling. In sprays all these interactions could occur leading to a 4-way coupling.

The Lagrangian and Eulerian representations The phases in a multiphase flow are usually represented using the Eulerian or Lagrangian frameworks. The

continuous phase is represented in the Eulerian frame and the dispersed phase can be represented either in the Eulerian or the Lagrangian frame depending on the multiphase modelling method used. A schematic of the streamline of a fluid particle is shown in Figure 2.1. In the Lagrangian frame the fluid particle is followed in

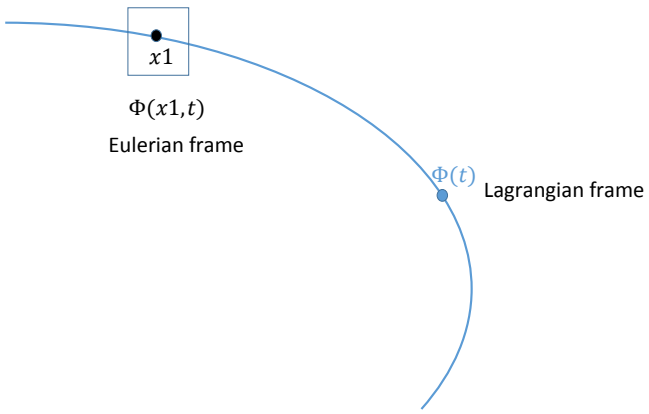

Figure 2.1: Lagrangian and Eulerian representations.

time. ϕ is any property of the fluid (temperature, size etc.). In the Eulerian frame, a control volume is chosen and the behavior of the particle at a given position x_1 is studied. Lagrangian method is useful for studying the dispersed phase where droplets for example can be tracked in time. This approach is not feasible for the continuous phase as it's difficult to track, and therefore the Eulerian frame is used to represent the continuous phase. The rate of change of a vector property ϕ in the Eulerian frame is given by Eq. 2.2.

$$\frac{D\boldsymbol{\phi}}{Dt} = \frac{\partial \boldsymbol{\phi}}{\partial t} + \sum \frac{\partial \boldsymbol{\phi}}{\partial x_i}\frac{\partial x_i}{\partial t} = \sum u_i \frac{\partial \boldsymbol{\phi}}{\partial x_i} \tag{2.2}$$

where the summation is over all the components of the vector ϕ. In vector notation the same equation can be written as

$$\frac{D\boldsymbol{\phi}}{Dt} = \frac{\partial \boldsymbol{\phi}}{\partial t} + \boldsymbol{u}.\nabla\boldsymbol{\phi} \tag{2.3}$$

For the continuous phase conservation equations are solved in the Eulerian frame, some of the important equations are: mass, momentum, energy and species conservation. The conservation equations are solved by 3 possible methods: Reynolds Averaged Navier Stokes (RANS), Large Eddy Simulations (LES) and Direct Numerical Simulations (DNS). These are in the increasing order of computational cost and decreasing order of modelling effort for a given problem. RANS solves only for the mean values of flow variables. The non-linear term (Reynolds stress) appearing in the momentum equation is closed by turbulence models. In LES only turbulent scales below a specified filter size are modelled, the rest of the scales are resolved and in DNS all the scales are resolved. All the simulations done in this work are RANS simulations.

Methods for modelling dispersed multiphase flows A classification and explanation of the methods for modelling dispersed multiphase systems is given here. Focus of this discussion is on fuel sprays, where liquid droplets are dispersed in gas. It should be pointed out that this is not a very strict classification and it does not cover all the methods but still covers a broad range of methods used. The intention of the author is to proved an overview of the modelling methods. A schematic of the classification is given in Figure 2.2. Broadly modelling approaches for solving

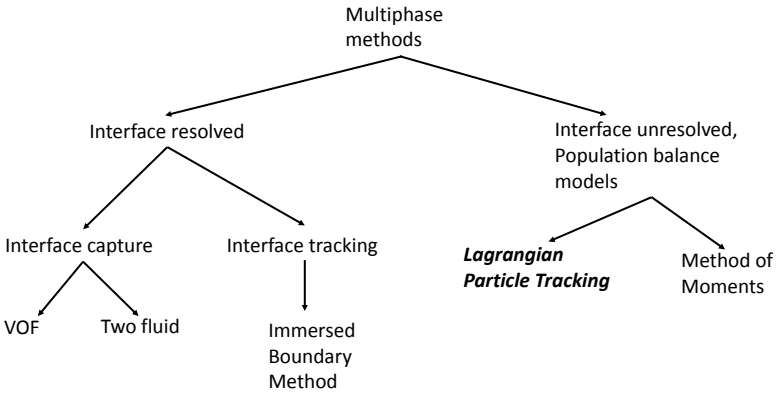

Figure 2.2: Classification of multiphase methods. The method used in this work is highlighted.

dispersed multiphase systems can be divided into interface resolved and interface unresolved methods.

Interface resolved methods In the interface resolved methods details of processes occurring at the interface are taken into account apart from the continuous and dispersed phase equations. These methods can be further classified as interface capturing and interface tracking methods. In interface tracking methods, the interface is represented by a separate computational mesh either in a Eulerian-Eulerian framework by a moving mesh representing the interface [57] or by Eulerian-Lagrangian framework by a separate Lagrangian framework that tracks the interface [29]. These methods provide accuracy in terms of describing the interface shape, but lack robustness in terms of interface deformation. Another example of method in interface tracking is the Immersed Boundary Method, which leaves out details of interface deformation and flow inside the dispersed phase (only considering global mass, momentum and energy exchange). This makes it computationally less expensive (e.g. [42]). The second class of interface resolved methods are the interface capturing methods. Here the interface is represented by a scalar field which is transported as the other physical variables. Examples are the Volume Of Fluid (VOF) and the Level Set method. A brief description of the VOF is now given.

Volume Of Fluid Method In the VOF method [61], volume fraction of the dispersed phase is defined and solved as a transport equation. The volume fraction

α is 1 for pure dispersed phase, 0 for pure continuous phase and a value in between indicates that a fractional volume of the cell is occupied by the dispersed phase which means there is an interface. The transport equation for α is then solved, it is given by Eq. 2.4

$$\frac{\partial \alpha}{\partial t} + \nabla . \alpha u = S_\alpha \tag{2.4}$$

The VOF is a mixed-fluid approach where a single set of momentum conservation equations is solved for the flow mixture rather than solving 1 for each phase. u in Eq. 2.4 is therefore velocity of the mixture. There is another type of model following the separate fluid approach, where both the continuous and dispersed phase comprise of two separate but intermixed continua. Two sets of momentum equations are therefore required: one for each phase. This method is often called the two-fluid method (Chapter 13.1.4.2, [9]).
To summarize, the interface resolving methods provide more accurate details of the interface, require high numerical resolution in time and space to resolve the interfaces and are often combined with LES or DNS simulations. They provide a lot of insight but are numerically expensive and not feasible for simulating practical problems such as fuel sprays in engines.

Interface unresolved In this category of methods , details of the interface are left out. The focus here is to not understand the processes at the interface. And to add a further level of simplicity, details of individual particles are also not taken into account. Rather, in this class, the behavior of a population of particles is taken into account. These class of models are known as population balance models (Chapter: Introduction and fundamentals of modeling approaches for polydisperse multiphase flows in [43]).

Population balance models In these models, the dispersed phase is represented as a population of discrete elements. If $\boldsymbol{\xi}$ denotes the internal coordinate vector of the particle representing its physical properties (e.g. particle size, temperature etc.) then the concentration of particles lying within the interval $[\boldsymbol{\xi}, \boldsymbol{\xi} + d\boldsymbol{\xi}]$ is given by the Number Density Function (NDF) denoted by $n_{\boldsymbol{\xi}}$. The NDF characterizes the dispersed phase population. Transport equations are now needed to be solved for the NDF in order to model the interactions of the dispersed phase with the continuous phase. The Population Balance Equation (PBE) is given by Eq. 2.5

$$\frac{\partial n_{\boldsymbol{\xi}}}{\partial t} + \nabla_x . (\mathbf{u} n_{\boldsymbol{\xi}}) + \nabla_{\boldsymbol{u_d}} . (\dot{\boldsymbol{u}}_{\boldsymbol{d}} n_{\boldsymbol{\xi}}) + \nabla_{\boldsymbol{\xi}} . (\dot{\boldsymbol{\xi}} n_{\boldsymbol{\xi}}) = S_{\boldsymbol{\xi}} \tag{2.5}$$

where the first term is the rate of change of droplets, the second term is the advection of droplets in physical space, the third term is the advection in the velocity space, the fourth term is advection of droplets in the phase space due to continuous processes and the last term on the RHS is the source term due to discontinuous processes such as collision. The third term appears in the equation because the droplet velocity is separated from the internal coordinates.

A numerical solution to PBE is possible using finite difference or finite volume methods but it computationally very expensive for practical applications. There are methods to calculate approximate solutions to the PBE these methods are now discussed.

Lagrangian Particle Tracking (LPT) One of the most popular method to provide approximate solution to the PBE is the LPT. LPT is a stochastic-parcel method. For a spray consisting of a large number of droplets, only the behavior of a subset of all the droplets is considered (Monte-Carlo approach). Each entity in subset is called a parcel. However in order to keep the correct fuel mass in the cylinder (in case of fuel sprays), each parcel gets a number of further droplets with identical properties. One parcel represents a random interval in a multivariate NDF. The parcels are tracked individually and equations are solved for mass, momentum and energy transfer. The transfer of these properties are included in the source terms which are then coupled to the gas phase. The source term contribution is then summed up for all the parcels in any given computational grid cell. In this work, the LPT method is followed. Details of the conservation equations for the parcels are discussed in Chapter 3.2. The advantage of LPT is that it is easily coupled to gas phase and can be solved with the RANS method which can be computationally efficient and be used to solve practical simulations. One of the disadvantages is that since this method is based on parcels, when large number of parcels are required, computational costs will increase. Another challenge is that computational cells with high liquid volume fraction have to be treated carefully.

Quadrature-Based Moment Methods (QBMM) The PBE discussed earlier has a high dimensionality for practical spray applications making the computation impractical. The QBMM (Chapter: Quadrature method of moments for polydisperse flows in [43]) is a family of methods developed to address this problem and it is a type of Moment Methods. In the QBMM method, instead of solving the PBE for all the internal coordinates, only the moments of a few coordinates are taken to represent the continuous-dispersed phase interactions. While method has the benefit of representing the dispersed phase in the Eulerian framework, the computational cost of increasing the number of representative internal coordinates is high.

This section has provided a brief but broad classification of multiphase modelling methods. As mentioned earlier, the focus of this work is on fuel sprays which are two phase systems consisting of droplets dispersed in surrounding gas. The dispersed phase is modelled using the Lagrangian Particle tracking method and the continuous phase uses RANS method to solve the conservation equations. Turbulence is modelled using the $k - \epsilon$ model. Hereafter all the discussion is focussed on fuel sprays (and a spray by default would refer to a fuel spray).

2.3 Structure of a spray

Figure 2.3 shows a representative picture of a spray from the simulations performed in this work. The simulation from which this picture was generated was performed

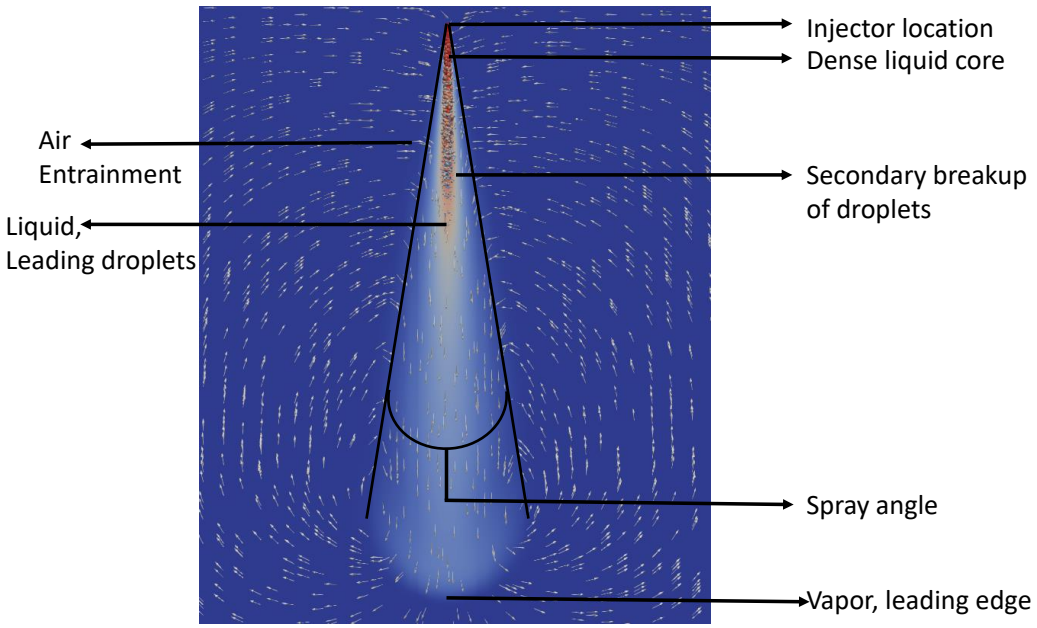

Figure 2.3: Evaporating fuel spray.

under diesel engine-like pre-combustion conditions with an ambient temperature and pressure of 900 K and 60.5 bar, and an injection pressure of 1500 bar. Fuel is injected at this high pressure from the injector and enters the combustion chamber at high velocities (600 m/s or more), forming a conical spray. The liquid jet then undergoes breakup into smaller droplets. Breakup can be conceptually divided into primary and secondary breakup. Primary breakup happens first and generates large ligaments and droplets that form a dense liquid core near the nozzle. The subsequent breakup of these droplets is known as secondary breakup. The smaller droplets created by secondary breakup can be seen in the figure. Secondary breakup is driven by the aerodynamic drag acting on the droplet. Liquid droplets may also collide or coalesce. The broken down droplets then evaporate and mix with the surrounding air to form fuel vapor. The distance of the leading droplets (shown in Figure 2.3) from the injector is called the liquid penetration and the distance of the leading edge of the vapor from the injector is called the vapor penetration. Different metrics may be used to characterize penetration lengths when considering different experimental measurements. The angle formed between the tangents to the outer peripheries of the spray is called the spray angle. Air entertainment is indicated by the arrows in the figure, which represent gas velocity vectors (the vectors are not sized by magnitude). The gas motion is caused by the transfer of momentum from the liquid, and the resulting turbulence (eddies) interact with the liquid spray, giving rise to so-called spray-turbulence interaction. Some of the physical processes mentioned here are discussed further in the subsequent sections.

2.4 Primary breakup

Primary breakup determines the initial conditions experienced by droplets entering from the nozzle. Quantities such as the initial radius, injection velocity, and spray angle are determined by primary breakup. While detailed models can be used to simulate primary breakup (and also simulate flows in the nozzle), this is computationally expensive. Experimental study of droplets close to the injector in the dense spray region is also challenging, so there is a lack of data that could be used to validate primary break-up models. One simple and popular method for determining initial droplet conditions is the so-called blob method.

Blob-method

The blob method was originally developed for full-cone sprays and describes the initial conditions of the droplets exiting the injector ([54], [55]). According to this model, atomization and droplet break-up within the dense spray near the nozzle are indistinguishable processes, so a detailed spray simulation can be replaced by assuming the injection of spherical droplets with uniform size which then undergo secondary breakup driven by aerodynamic forces (Figure 2.4). Each liquid blob is

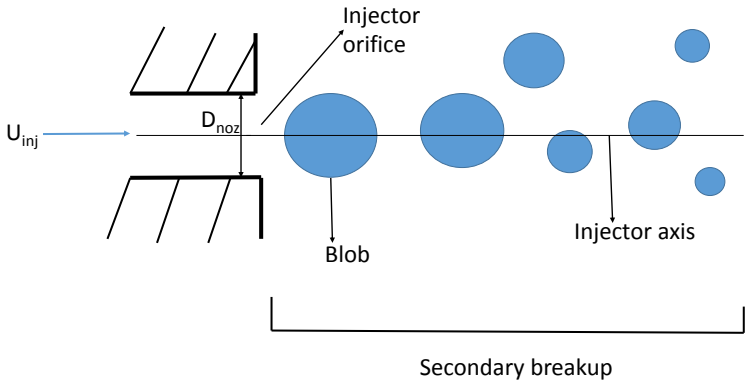

Figure 2.4: The blob method.

a computational unit consisting of a collection of droplets whose properties can be identified. Blobs are used to make computational calculations easier. The injected blobs have the same diameter as the injector orifice, and the conservation of mass in the nozzle gives Eq. 2.6.

$$U_{inj}(t) = \frac{\dot{m}_{inj}(t)}{A\rho_l} \tag{2.6}$$

where m_{inj} is the injection mass flow rate (vs. time) and is obtained either from experimental data or modelled, A is the nozzle orifice area, and ρ_l is the fuel density. The direction of the blobs is determined by the injection velocity and the spray cone angle, specified as an input, or derived from experimental data.

2.5 Secondary breakup

Secondary breakup is the process by which injected droplets fragment into smaller ones because of aerodynamic forces resulting from the different velocities of the gas and the liquid. These aerodynamic forces are opposed by surface tension, which acts to preserve the spherical form of the droplets. The relationship between these two forces is described by the dimensionless Weber number (Eq. 2.7).

$$We_g = \frac{\rho_g U_{rel}^2 d}{\sigma} \tag{2.7}$$

where d is the droplet diameter and σ is the surface tension of the fuel. The Weber number is often used to describe secondary breakup; a higher We indicates stronger secondary breakup. Several different breakup modes exist, each associated with different ranges of We values. Some secondary breakup models use these modes to determine droplet breakup time and droplet size [49]. Models of this type are called phenomenological models because they are based on semi-empirical relationships for breakup times. There are also other breakup models such as the Taylor Analogy Breakup (TAB) model, which is based on an analogy between a forced oscillating spring-mass system and an oscillating droplet that penetrates into a gaseous atmosphere. The Kelvin- Helmholtz (KH) Breakup model is another secondary breakup model proposed by Reitz [54], which is based on a first order linear analysis of KH instability growing on the surface of a liquid jet that is penetrating into a gaseous atmosphere with a relative velocity U_{rel}. The Rayleigh-Taylor (RT) breakup model is based on instability arising at the interface between the liquid and the gas, and assumes that the instability waves cause liquid droplet breakup. For a detailed discussion of the TAB, KH, and RT models, the reader is referred to the work of Baumgarten [7], Chapter 4.2. The phenomenological model based on Pilch and Erdman correlations [49] is discussed at more length in Chapter 3.

2.6 Spray turbulence interaction

In addition to being the source of drag force between the gas and the liquid droplets, the relative velocity also causes droplet dispersion or diffusion due to turbulent velocity fluctuations of the gas. This accelerates mixing of air and fuel and generates a more homogeneous mixture than would be obtained under laminar flow conditions. The gas velocity in a turbulent flow is the sum of a time or ensemble averaged (mean) component and a fluctuating component as shown in Eq. 2.8

$$\vec{u} = \vec{\bar{u}} + \vec{u'} \tag{2.8}$$

The fluctuations are assumed to be isotropic (i.e. the turbulence is assumed to be the same in all directions). The value of the fluctuating component $\vec{u'}$ is sampled from a Gaussian distribution given by Eq. 2.9

$$G(u') = \frac{1}{\sqrt{2\pi}\sqrt{\frac{2k}{\epsilon}}} e^{\left(\frac{|u'|^2}{\frac{4k}{3}}\right)} \tag{2.9}$$

where k is the turbulent kinetic energy and ϵ is turbulent dissipation. The variance of the distribution is equal to the turbulence intensity (Eq. 2.10).

$$\sigma = |u'| = \sqrt{\frac{2k}{3}} \tag{2.10}$$

2.7 Modelling of multicomponent fuel sprays

Multicomponent spray models fall in two main categories: discrete and continuous [7]. In discrete models ([3], [52], [50], [68]), each fuel component is tracked separately. In a continuous model ([10], [74], [40], [39]) a continuous distribution function f(I) characterizes the distribution of macroscopic property I of the mixture (e.g. its molecular mass or boiling point). This method was developed by Tamin and Hallet [64] using the continuous thermodynamic model. The continuous thermodynamic model then solves three equations (one representing the multicomponent fuel and 2 for the mean and variance of the distribution function). Discrete and continuous models each have their own pros and cons. Discrete models can accurately characterize a multicomponent fuel and enable easy coupling to chemical kinetics but can become computationally expensive as the number of components to model increases. [68] cited in the beginning of this section used the discrete model of [52] to model the physical properties of a multicomponent surrogate gasoline fuel to study fuel components vapor distribution and coupled the spray model to a surrogate gasoline chemical mechanism to predict the effect of multicomponent fuel composition on boiling temperature and ignition delay. Another example from the same group is [36] where a 10 component gasoline fuel was simulated in GDI engine and constant volume chamber configurations for cold start conditions. Vapor distribution of the components were compared with experiments. Continuous models are computationally less demanding but require greater modelling effort and also introduce additional tuning parameters due to the use of Gamma functions. Another important drawback is that components belonging to different groups (e.g. alkanes and aromatic compounds) cannot be modeled with a single distribution function. Yang [72] developed a hybrid discrete and continuous multicomponent model in which gasoline was assumed to consist of a family of five hydrocarbons. Each family was in turn assumed to consist of an infinite number of continuous compounds represented by a probability density function (pdf), the mass fraction of each of family was represented by another pdf; the mean and variance of each pdf were tracked. Another example implementing a hybrid multicomponent model is [56]. [20] also used the method introduced by [72] to validate the multicomponent model for evaporation of diesel fuel droplets. Both [52] and [72] modelled realistic fuels (gasoline and diesel in the case of [52], and gasoline in the case of [72]) and obtained results in good agreement with experiment. [51] used a quasi-discrete model where alkane components with close carbon numbers n were replaced by a new alkane component with an average value of n, taking into account the mole fractions of the original components. The spray model used in this work is a discrete multicomponent model. Details of implementation is given in Chapter 3.

2.8 Vapor Liquid Equilibrium (VLE)

Ideal VLE VLE is attained when the saturated pressure of the liquid is equal to its vapor pressure, resulting in an equilibrium state for the evaporation of the liquid. VLE exists when Eq. 2.11 (known as the Raoult's law) is satisfied.

$$P_{i,v} = X_{i,v} P_{gas} = X_{i,l} P_{sat,i}(T_{gas}) \tag{2.11}$$

where $P_{i,v}$ is the vapor pressure of fuel component i, $X_{i,v}$ is the mole fraction of fuel component i in the gas phase, $X_{i,l}$ is the mole fraction of fuel component i in the liquid fuel mixture , P_{gas} is the gas pressure and $P_{sat,i}$ is the saturation pressure of fuel component i at the gas temperature. Rearranging Eq. 2.11 and replacing the mole fraction in terms of the mass fraction, we get Eq. 2.12, which is another form of the same law.

$$y_{fu,eq,i} = \frac{M_{fu,i}}{M_{mix}} \frac{P_{sat,i}(T_{gas})}{P_{gas}} X_{i,l} \tag{2.12}$$

Here, $y_{fu,eq,i}$ is the equilibrium vapor mass fraction for fuel component i, M_{mix} is the molecular weight of the gas mixture, and $M_{fu,i}$ is the molecular weight of fuel component i. Raoult's law assumes ideal thermodynamics and therefore does not take into consideration the intermolecular forces between fuel molecules.

Non-ideal VLE The ideal Raoult's law assumption is reasonable for single component fuels but leads to deviation in the prediction of VLE for multicomponent fuels especially those containing polar molecules [6]. When polar molecules (found in alcohols like ethanol) are blended with straight chain molecules like alkanes, the fuel's behavior deviates strongly from ideality, and the magnitude of this deviation increases with the blend's alcohol content.
Non-ideal VLE is achieved if the fugacity of the vapor is equal to that of the liquid for each of the component. There are two approaches to determine fugacities. One is using the equation of state models and the other is using excess functions (excess Gibbs energy for example) where excess functions are used to represent the deviations from ideality. Examples of equation of state models are virial, Lee-Kesler, and two parameter cubic equation of state such as van der Waals, Redlich-Kwong (RK), Peng-Robinson (PR). Examples of excess function method are non random two liquid (NRTL) model, Wilson method and universal quasi-chemical functional group activity coefficients (UNIFAC) model. [32], [73], [33] used PR method, [27], [46] used UNIFAC method and [6], [35] used NRTL method. Each method has its own benefits. The NRTL method, based on Scott's two liquid theory, has been proven to hold for a wide range of mixtures with minimal assumptions and adjustable parameters [58]. In this work the NRTL method is used to calculate fugacities. The non-ideal VLE is implemented in the spray model and applied for a simulation case using an alcohol fuel blend. The influence of non-ideal VLE on spray formation is then studied. This topic is discussed at greater length in Chapter 3.

Chapter 3

Methodology and modelling approach

Spray formation involves interactions between the liquid and gas phases. The gas phase is solved using the Eulerian approach and the liquid phase is solved using the Lagrangian approach. This chapter describes the methods used for solving both the phases and their interactions.

3.1 The Eulerian phase

The gas phase is solved using the Eulerian approach in which transport equations are solved for the conversation of mass, energy and momentum of the gas in the grid cells of the computational domain. The equations are written using Reynold's average for density and pressure and Favre average for rest of the variables. Eq. 3.1 is the continuity equation used to solve for the conservation of mass.

$$\frac{\partial \bar{\rho}}{\partial t} + \nabla.(\bar{\rho}\widetilde{\mathbf{u}}) = \frac{\dot{S}_M}{V\Delta t} \tag{3.1}$$

The time-dependent source term $\dot{S}_M$ is obtained from the spray model. It represents mass transfer due to evaporation from the liquid phase, V is the grid cell volume and Δt is the computational time step. The momentum equation is given by Eq. 3.2.

$$\frac{\partial \bar{\rho}\widetilde{\mathbf{u}}}{\partial t} + \nabla.(\bar{\rho}\widetilde{\mathbf{u}}\widetilde{\mathbf{u}}) = -\nabla\bar{p} + \nabla.[(\mu+\mu_t)(\nabla\widetilde{\mathbf{u}} + (\nabla\widetilde{\mathbf{u}})^T)] - \nabla.[\frac{2}{3}(\mu+\mu_t)\nabla\widetilde{\mathbf{u}}] + \bar{\rho}g + \frac{\dot{S}_I}{V\Delta t} \tag{3.2}$$

Here $\dot{S}_I$ is the time dependent source term for momentum (transferred from the liquid phase) obtained from the spray model. μ is the laminar viscosity, μ_t is the turbulent viscosity and it is calculated from the turbulent kinetic energy and dissipation, obtained from the k-ϵ turbulence model which is discussed later in this chapter. The terms $\nabla.[(\mu+\mu_t)(\nabla\widetilde{\mathbf{u}} + (\nabla\widetilde{\mathbf{u}})^T)] - \nabla.[\frac{2}{3}(\mu+\mu_t)\nabla\widetilde{\mathbf{u}}]$ in Eq. 3.2 are calculated by the function: *divDevReff(U)* in OpenFOAM-2.2.x. Gravity is the only external force

considered in Eq. 3.2. The energy equation is given by Eq. 3.3

$$\frac{\partial \bar{\rho}\widetilde{h}}{\partial t} + \nabla.(\bar{\rho}\widetilde{\mathbf{u}}\widetilde{h}) = \frac{D\bar{p}}{Dt} + \nabla.((\alpha_l + \alpha_t)\nabla\widetilde{h}) + \frac{\dot{S_E}}{V\Delta t} + \bar{\rho}\dot{Q} \tag{3.3}$$

Here the time dependent source term $\dot{S_E}$ represents energy transfer from the liquid phase (obtained from the spray model) and $\dot{Q}$ is the time dependent specific energy source (e.g. heat from chemical reactions during combustion) per unit volume for the grid cell. In the spray simulations performed in this work only non-combusting cases are studied and therefore $\dot{Q} = 0$. α_l and α_t are the laminar and turbulent thermal diffusivities and they are calculated from the respective viscosities using the Prandtl number.

3.2 The Lagrangian phase - VSB2 model

The most common approach followed in numerical simulations of sprays is to use the Discrete Droplet Model [11] for solving the liquid and gas phases. The DDM uses an Eulerian-Lagrangian approach. The gas phase is solved using the Eulerian approach. The liquid phase is solved using the Lagrangian approach in which the parcels are tracked in time and space. A parcel is a computational unit consisting of liquid droplets with identical properties (e.g. size, temperature, velocity).
The spray model used for the simulations in this work, was the stochastic blob and bubble (VSB2) model. The model was developed and implemented by Karlsson and its first validation with experimental data is described in [31]. It is a Lagrangian model solving for the liquid phase. In contrast with the traditional Eulerian-Lagrangian approach, where the liquid fuel is represented by computational parcels containing identically sized droplets, the liquid fuel in the VSB2 model is represented by computational blobs. In each blob, the droplets are divided into a number of bins based on their size distribution, which is governed by a distribution function. The parameters of the distribution function are determined by the local conditions around each specific liquid blob at a given time instant. The blobs interact with the air in the surrounding bubble instead of the entire grid cell. This is done to reduce grid dependence especially when coarse grid cells are used. Further discussion on the bubble is given later. A schematic depiction of the blob and bubble concept is shown in Figure 3.1.

The VSB2 model solves primarily, for mass, momentum and energy transfer between the liquid phase and the surrounding gas. Relaxation equations are used to solve mass and heat transfer. The following sections describe some of the important physical processes modelled in VSB2.

3.2.1 Blob creation

Liquid blobs are injected with a blob diameter, D_{blob} and a blob mass m_{blob} given by Eq. (3.4).

$$m_{blob} = N_{rep}\rho_{liq}\frac{\pi}{6}D_{blob}^3 \tag{3.4}$$

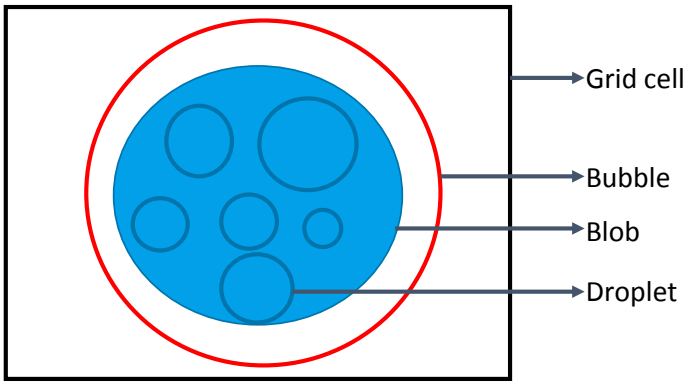

Figure 3.1: Blob and bubble concept.

where N_{rep} is a representative number used to maintain mass balance for a given blob with diameter D_{blob}. N_{rep} is constant throughout the blob's lifetime.

3.2.2 Primary breakup

In this work, the blob injection method was used to treat primary breakup (explained in Chapter 2.4) by injecting liquid blobs with the same diameter as the nozzle orifice.

3.2.3 Secondary breakup

Secondary breakup refers to the breakup of liquid droplets formed by atomization (primary breakup) into smaller ones. Secondary breakup occurs because of the drag force acting on the droplets, which originates from the difference in velocity between the droplets and the surrounding gas. As noted above, droplets are collected in computational units called blobs. The size of the blobs formed by secondary breakup is given by Eq. (3.5)

$$D'_{blob} = D_s + (D_{blob} - D_s)e^{\frac{-\Delta t}{\tau_{breakup}}} \tag{3.5}$$

where D'_{blob} is the blob diameter after breakup, D_{blob} is the initial blob diameter, D_s is the stable droplet diameter and Δt is the computational time step. $\tau_{breakup}$ is breakup time and it is obtained from the correlations of Pilch and Erdman (Pilch and Erdman, 1987). D_s is given by Eq. (3.6)

$$D_s = We_{cr}\sigma/(\rho_{gas}U^2_{rel}) \tag{3.6}$$

The critical Weber number We_{cr} is given by Eq. (3.7)

$$We_{cr} = 12(1 + 1.077Oh^{1.6}) \tag{3.7}$$

where Oh represents the Ohnesorge number, which is a function of the Reynolds and Weber number.

3.2.4 Stripped off mass

The stripped off mass is the liquid mass removed from the parent blob by secondary breakup. It is given by Eq. (3.8)

$$m_s = \rho_{liq}\frac{\pi}{6}(D_{blob}^3 - D_{blob}^{'3}) \tag{3.8}$$

where D_{blob} and $D_{blob}^{'}$ are the sizes of blob before and after breakup, respectively.

3.2.5 Droplet size distribution

The size distribution of droplets in a blob is represented by a one-parameter cumulative distribution function (CDF). The parameter f is called the power coefficient. The CDF takes the form given by Eq. (3.9)

$$D = M^f, M\epsilon[0,1], f > 0 \tag{3.9}$$

where $\{D\}$ and $\{M\}$ represent the normalized droplet size and mass, respectively. $\{D\}$ is a collection of n size intervals corresponding to $\{M\}$ which is a collection of n mass packages. The first mass package is the normalized stripped off mass M_{sn} and the corresponding size interval is the normalized stable droplet diameter D_{sn}. The remaining mass is divided equally in to $n-1$ mass packages. The remaining size intervals are calculated from the corresponding mass using Eq. (3.9). The power coefficient f is calculated from D_{sn} and M_{sn}. D_{sn} is given by Eq. (3.10)

$$D_{sn} = \frac{D_s}{D_{blob}} \tag{3.10}$$

M_{sn} is given by Eq. (3.11)

$$M_{sn} = \frac{m_s}{m_{blob}} = \frac{D_{blob}^3 - D_{blob}^{'3}}{D_{blob}^3} = 1 - (\frac{D'_{blob}}{D_{blob}})^3 \tag{3.11}$$

The power coefficient is then given by Eq. (3.12)

$$f = \frac{\log(D_{sn})}{\log(M_{sn})} = \frac{\log(\frac{D_s}{D_{blob}})}{\log[1 - (\frac{D'_{blob}}{D_{blob}})^3]} \tag{3.12}$$

Figure 3.2 shows an example plot of $\{D\}$ vs. $\{M\}$ where there are 10 size intervals ($n = 10$). The first mass package is M_{sn} and the corresponding size interval is D_{sn}. The remaining mass is divided equally into 9 mass packages and the remaining size intervals are calculated from the corresponding mass packages using Eq. 3.9.

3.2.6 Mass transfer

Mass transfer from the liquid to the gas phase is given by Eq. (3.13)

$$\frac{dm_{evap,i,j}}{dt} = \frac{m_{eq,j} - m_{blob,i,j}}{\tau_{m,i,j}} \tag{3.13}$$

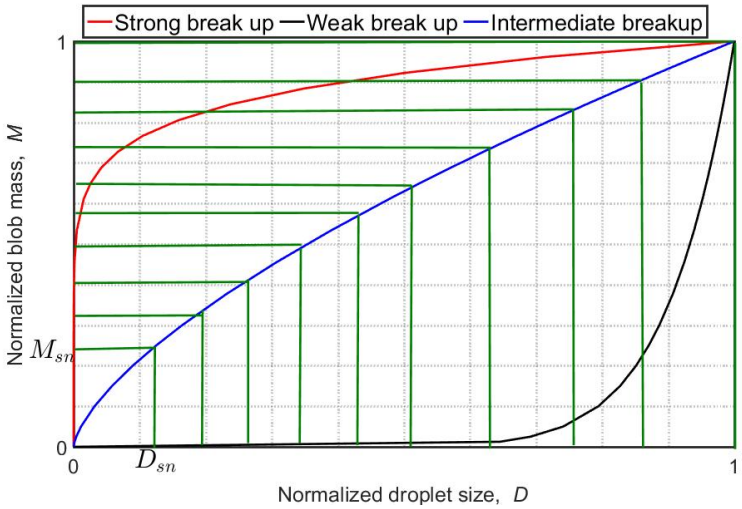

Figure 3.2: Cumulative droplet size distribution function.

where i denotes a specific mass package and j denotes a specific fuel component (in a multicomponent fuel mixture) for a given blob. $m_{eq,j}$ is the equilibrium mass for fuel component j (the mass evaporated under the given conditions until the gas is saturated, discussed further in Section 3.2.9) and $\tau_{m,i,j}$ is the evaporation time scale, which is given by Eq. 3.14.

$$\tau_{m,i,j} = \frac{\rho_l D_{blob,i}^2 R T_f (Y_{eq,j} - Y_{sc,j})}{6 P_{gas} D_j Sh} \tag{3.14}$$

Here, ρ_l is the liquid density, $D_{blob,i}$ is the diameter defined for size interval (mass package) i, T_f is the film temperature, $Y_{eq,j}$ is the maximum evaporated liquid mass fraction (fraction of the blob mass) until saturation for fuel component j, $Y_{sc,j}$ is the supercritically transferred mass fraction for fuel component j, D_j is the diffusion coefficient for fuel component j and Sh is the Sherwood number. When the gas temperature and pressure are above the critical values, mass transfer is assumed to be an instantaneous process, independent of time.

3.2.7 Heat transfer

The heat transfer from the surrounding gas (in the bubble) to the blob is given by Eq. (3.15)

$$\frac{dT_{blob}}{dt} = \sum_{i=1}^{n_{blob}} \frac{T_{eq} - T_{blob}}{\tau_{T,i}} \tag{3.15}$$

where n_{blob} is the number of size intervals (mass packages), T_{eq} is the equilibrium temperature of the blob-bubble system. T_{eq} is calculated in advance from the energy balance between the blob and the bubble after mass transfer has occurred. T_{blob} is the temperature of the blob and $\tau_{T,i}$ is the heat transfer time scale, which is given by Eq. 3.16.

$$\tau_{T,i} = \frac{\rho_l D_{blob,i}^2 C_{p,blob}}{6 \lambda Nuf} \tag{3.16}$$

λ is the thermal conductivity of the liquid film, f is the correction factor that accounts for the influence of heat transfer on the mass transfer coefficient as given by [15], and Nu is the Nusslet number which is a function of Reynold's and Prandtl number as given in [53].

3.2.8 Momentum transfer

The momentum equation for the blob is given by Eq. (3.17)

$$m_{blob}\frac{dU_{blob}}{dt} = \sum_{i=1}^{n_{blob}} \frac{\pi D_i^2}{8}\rho_g C_d V_R (U_g^{'} - U_{blob}^{'}) \tag{3.17}$$

where subscript i refers to a specific size interval, D_i is the diameter of droplets belonging to size interval i, V_R is the relative velocity at the old time step

$$V_R = |U_g^o - U_{blob}^o| \tag{3.18}$$

and $U_g^{'}$ and $U_{blob}^{'}$ are the gas and blob velocities at the new time-step. C_d in Eq. (3.17) is the drag coefficient, C_d at Reynolds numbers up to 2000 is given by Eq. (3.19) as suggested by [62].

$$\begin{aligned} C_d \;=\; & 0.28 + \frac{21}{Re_i} + \frac{6}{\sqrt{Re_i}} + \\ & + We\,(0.2319 - 0.1579\,log\,(Re_i) + \\ & + 0.0471\,log^2\,(Re_i) - 0.0042\,log^3\,(Re_i)) \end{aligned} \tag{3.19}$$

The equation for C_d accounts for droplet deformation in the subcritical Weber number range. At higher Reynolds numbers, Cd is equal to 0.424. The momentum transferred from the liquid blob to the gas is given by Eq. (3.20)

$$m_g\frac{dU_g}{dt} = -m_{blob}\frac{dU_{blob}}{dt} \tag{3.20}$$

Substituting Eq. (3.20) into Eq. (3.17) gives an expression for the blob velocity in the new time step.

3.2.9 Calculation of equilibrium mass

The equilibrium mass is the mass of liquid that can evaporate under given pressure and temperature conditions before the surrounding gas is saturated. A schematic depiction of the evaporation of a blob is given in Figure 3.3.

Heat is transferred from the surrounding gas (bubble) to the blob, causing it to evaporate. Evaporation of each fuel component proceeds until its saturated mass fraction is reached. The saturated fuel mass fraction is calculated using Eq. (3.21)

$$Y_{fu,sat,i} = \frac{M_{fu,i}}{M_{mix}}\frac{P_{sat,i}(T)}{P}X_{liq,i} \tag{3.21}$$

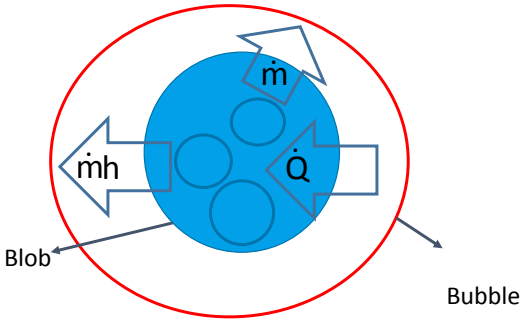

Figure 3.3: Evaporation of a blob in a bubble.

where $Y_{fu,sat,i}$ is the saturated mass fraction for fuel component i, $M_{fu,i}$ is the molecular weight of fuel component i, M_{mix} is the molecular weight of the mixture in the gas phase, $P_{sat,i}$ is the saturated vapor pressure of fuel component i, P is the gas pressure, T is the bubble temperature and $X_{liq,i}$ is the mole fraction of fuel component i in the liquid droplet. Eq. 3.21 represents ideal Vapor Liquid Equilibrium (VLE) and is known as Raoult's law. Non-ideal VLE is discussed later.

During evaporation, mass and enthalpy are transferred to the bubble. The change in the mass fraction and enthalpy of the bubble in turn changes it's temperature. Evaporation thus alters bubble enthalpy and temperature as well as the mass fraction of all species in the bubble. These processes are represented by Eqs. (3.22 - 3.24)

$$Y_i' = \frac{y_i m + \Delta m_i}{m + \sum_1^{N_f} \Delta m_i} \tag{3.22}$$

$$h_g' = \frac{m h_g + \sum_1^{N_f} \Delta m_i [h_{fuel,vap,i}(T_{dr}) - \Delta h_{vap,i}(T_{dr})]}{m + \sum_1^{N_f} \Delta m_i} \tag{3.23}$$

$$h_g'(T) = \sum Y_i' h_i(T) \tag{3.24}$$

where Δm_i is the mass of fuel component i that has evaporated until saturation (equilibrium mass); Y_i', h_g', and T' are the updated mass fraction, enthalpy and temperature respectively for the gas phase. N_f is the number of fuel components, $h_{fuel,vap,i}$ and $\Delta h_{vap,i}$ are the fuel vapor enthlapy and the enthalpy of vaporization of fuel component i, respectively, at the droplet temperature. Eq. (3.24) is a function that computes the gas temperature from the gas enthalpy and the mass fraction of species in the gas. The set of non-linear equations shown above are coupled (Eq. 3.21 - 3.24), and solved simultaneously using the SUNDIALS' KINSOL solver [8]. SUNDIALS is a software package providing time integrators and non-linear solvers that can be coupled with CFD codes. KINSOL is the solver package used in SUNDIALS to solve non-linear algebraic equation systems. The solution to the above-mentioned equations yields the equilibrium mass Δm for all the fuel components, which is then used as m_{eq} in Eq. (3.13).

3.2.10 The bubble approach

To minimize grid dependency, the blob was assumed to interact with a surrounding volume enclosed by a bubble (study on influence of using the bubble is performed in PaperIII). The volume of the bubble is less than or equal to that of the grid cell; for larger grid cells, the bubble volume is much smaller than the grid cell. The bubble size controls the rate of evaporation in large grid cells. The volume of the bubble is given by Eq. (3.25).

$$V_{bub} = \rho_g N_D \frac{\pi}{4} D_e^2 l_{diff} \tag{3.25}$$

where N_D is the actual number of droplets in the blob and D_e is the effective diameter of the droplets in the blob. It is given by Eq. (3.26)

$$D_e = \sum_{i=1}^{n_{blob}} \frac{m_i}{m_{blob}} D_i \tag{3.26}$$

where n_{blob} is the number of size intervals and D_i is the diameter defined for size interval i. N_D is calculated from D_e using an expression similar to Eq. (3.4).
l_{diff} in Eq. (3.25) is the turbulent length scale, which is based on turbulent diffusion and it is given by Eq 3.27

$$l_{diff} = \sqrt{\frac{\mu_t}{\rho_g} dt_s} \tag{3.27}$$

Here, μ_t is the turbulent viscosity and dt_s is the sub time-step (the time step spent by a blob in a grid cell).

3.2.11 Turbulence modelling

The turbulence model used for the gas phase in this work is the standard two equation $k-\epsilon$ model which is used to model the unclosed terms in the Reynolds stresses arising from the momentum equation (Eq. 3.2). The underlying assumption is based on Boussinesq hypothesis which states the momentum transfer in turbulent flow is dominated by mixing caused by turbulent eddies. It gives an expression to calculate the Favre averaged Reynolds stress tensor as given by Eq. 3.28.

$$\widetilde{\tau} = -\bar{\rho}\widetilde{\mathbf{u}''\mathbf{u}''} = \mu_t[\nabla\widetilde{\mathbf{u}} + (\nabla\widetilde{\mathbf{u}}^T) - \frac{2}{3}\nabla\widetilde{\mathbf{u}}] - \frac{2}{3}\bar{\rho}\widetilde{k} \tag{3.28}$$

The last term in the right hand most side of the equation, $-\frac{2}{3}\bar{\rho}\widetilde{k}$ is usually neglected to simplify the turbulence models. This expression of Reynolds stress tensor is then plugged in to the momentum equation (Eq. 3.2). Now in order to completely close the momentum equation, the turbulent viscosity μ_t in Eq. 3.28 needs to be known and it is given by Eq. 3.29

$$\mu_t = C_\mu \bar{\rho} \frac{\widetilde{k}^2}{\widetilde{\epsilon}} \tag{3.29}$$

$\widetilde{k}$ and $\widetilde{\epsilon}$ are obtained by solving two additional transport equations. The k-ϵ model was originally developed for incompressible flows [28] and then subsequently modified

to describe compressible flows [19]. The transport equation for the turbulent kinetic energy k, is given by Eq. (3.30)

$$\frac{\partial \bar{\rho}\widetilde{k}}{\partial t} + \nabla(\bar{\rho}\widetilde{k}\widetilde{\mathbf{u}}) = \nabla[(\frac{\mu_t}{\sigma_k} + \mu)\nabla\widetilde{k}] + \mu_t[\widetilde{\mathbf{S}} - \frac{2}{3}(\nabla\widetilde{\mathbf{u}})^2] - \frac{2}{3}\rho\widetilde{k}\nabla\widetilde{\mathbf{u}} - \bar{\rho}\widetilde{\epsilon} \tag{3.30}$$

where the first two terms on the L.H.S are rate of change of $\widetilde{k}$ and transport of $\widetilde{k}$ by convection, first term on the R.H.S is the transport of $\widetilde{k}$ by diffusion, second and third terms contribute to the rate of production of $\widetilde{k}$ and the last term contributes to the rate of destruction of $\widetilde{k}$. The transport equation for dissipation of the turbulent energy ϵ is Eq. (3.31)

$$\frac{\partial \bar{\rho}\widetilde{\epsilon}}{\partial t} + \nabla(\bar{\rho}\widetilde{\epsilon}\widetilde{\mathbf{u}}) = \nabla[(\frac{\mu_t}{\sigma_\epsilon} + \mu)\nabla\widetilde{\epsilon}] + \mu_t C_1\frac{\widetilde{\epsilon}}{\widetilde{k}}[\widetilde{\mathbf{S}} - \frac{2}{3}(\nabla\widetilde{\mathbf{u}})^2] - \frac{2}{3}(C_1 + C_3)\bar{\rho}\widetilde{\epsilon}\nabla\widetilde{\mathbf{u}} - C_2\bar{\rho}\frac{\widetilde{\epsilon}^2}{\widetilde{k}} \tag{3.31}$$

where the first two terms on the L.H.S are rate of change of $\widetilde{\epsilon}$ and transport of $\widetilde{\epsilon}$ by convection, first term on the R.H.S is the transport of $\widetilde{\epsilon}$ by diffusion, second and third terms contribute to the rate of production of $\widetilde{\epsilon}$ and the last term contributes to the rate of destruction of $\widetilde{\epsilon}$. $\widetilde{\mathbf{S}}$ is the strain rate tensor and it is given by Eq. (3.32)

$$\widetilde{\mathbf{S}} = 2\widetilde{\mathbf{S}}_{\mathbf{ij}}\widetilde{\mathbf{S}}_{\mathbf{ij}} = \frac{1}{2}(\frac{\partial\widetilde{\mathbf{u_j}}}{\partial x_i} + \frac{\partial\widetilde{\mathbf{u_i}}}{\partial x_j})^2 \tag{3.32}$$

Few terms in the $\widetilde{k}$ and $\widetilde{\epsilon}$ equations are lumped together in to one tensor in the OpenFOAM-2.2.x implementation as given by Eq. 3.33

$$G = \mu_t[\widetilde{\mathbf{S}} - \frac{2}{3}(\nabla\widetilde{\mathbf{u}})^2] \tag{3.33}$$

3.3 Vapor-liquid equilibrium

Vapor liquid equilibrium (VLE) is the steady state condition that is reached when the saturation vapor pressure of liquid and vapor pressure of fuel are equal. Evaporation stops when this condition is reached. VLE is usually given by Raoult's law, which assumes ideal thermodynamics (Eq 3.21). This assumption means that intermolecular interactions are neglected, which greatly simplifies the modeling of VLE and works reasonably well for single component fuels. However, strong deviations from ideal behavior are observed with multicomponent fuels, especially those that contain polar molecules (notably, alcohols such as ethanol) blended with straight chain alkanes. Moreover, the magnitude of this deviation increases with the fuel's alcohol content. It is therefore needed to consider non-ideal VLE.

Non-ideal VLE occurs when the fugacities of the vapor and liquid phases are equal. The liquid fugacity is a function of (among other parameters) the activity coefficient γ, which takes into account the intermolecular forces between different

kinds of molecules in a fuel blend. γ is computed using the Non-random two liquid (NRTL) method (Eq 3.34).

$$\ln \gamma_i = \frac{\sum_{j=1}^{K} X_{j,l} G_{ji}(T) \tau_{ji}(T)}{\sum_{k=1}^{K} X_{k,l} G_{ki}(T)} + \sum_{j=1}^{K} \frac{X_{j,l} G_{ji}(T)}{\sum_{k=1}^{K} X_{k,l} G_{kj}(T)} (\tau_{i,j}(T) - \frac{\sum_{n=1}^{K} X_{n,l} G_{ni}(T) \tau_{ni}(T)}{\sum_{n=1}^{K} X_{k,l} G_{kj}(T)}) \tag{3.34}$$

where the binary coefficients $G_{i,j}$ and $\tau_{i,j}$ are given by

$$G_{i,j} = e^{-\alpha_{i,j} \tau_{i,j}} \tag{3.35}$$

$$\tau_{i,j} = A_{i,j} + \frac{B_{i,j}}{T} \tag{3.36}$$

$$\alpha_{i,j} = C_{i,j} + D_{i,j} \tag{3.37}$$

The coefficients $A_{i,j} - D_{i,j}$ are obtained from the database of the chemical engineering software suite, Aspen plus. They are based on experimental data but can also be determined by UNIQUAC Functional-group Activity Coefficients (UNIFAC) method [17].

In NRTL method, excess thermodynamic functions (such as the Gibbs free energy) are used to express deviations from ideal VLE. For further details, the reader is referred to the work of Renon and Prausnitz [58]. The NRTL method is used in this work because it has been tested for a wide range of mixtures and also involves fewer assumptions and adjusting parameters than other non-ideal VLE models.
Taking the activity coefficient γ into consideration, the modified Raoult's law for non-ideal thermodynamic equilibrium is obtained (Eq 3.38)

$$y_{fu,eq,i} = \frac{M_{fu,i}}{M_{mix}} \frac{P_{sat,i}(T_{bub})}{P} X_{i,l} \gamma_i \theta_i \tag{3.38}$$

θ_i in Eq. 3.38 is the gas phase correction factor. At moderate pressures (relevant to the operating pressure conditions considered in this work) θ_i can be assumed to be unity [35]. $y_{fu,eq,i}$ from Eq. 3.38 is used instead of the ideal Raoult's law (Eq. 3.21) to calculate the equilibrium mass.

3.3.1 VLE for ethanol/iso-octane blend

To illustrate the influence of non-ideal thermodynamics, VLE was computed for an ethanol/iso-octane blend at atmospheric pressure is calculated using Eq 3.39

$$P = \sum P_{vap,i}(T) X_{i,l} \gamma_i \tag{3.39}$$

Here, P is mixture pressure and $P_{vap,i}$ is the saturated vapor pressure of each component. The mixture pressure is fixed at 1.013 bar. The equilibrium composition at different temperatures was computed using Eq 3.39 and the results are plotted in Figure 4.6.

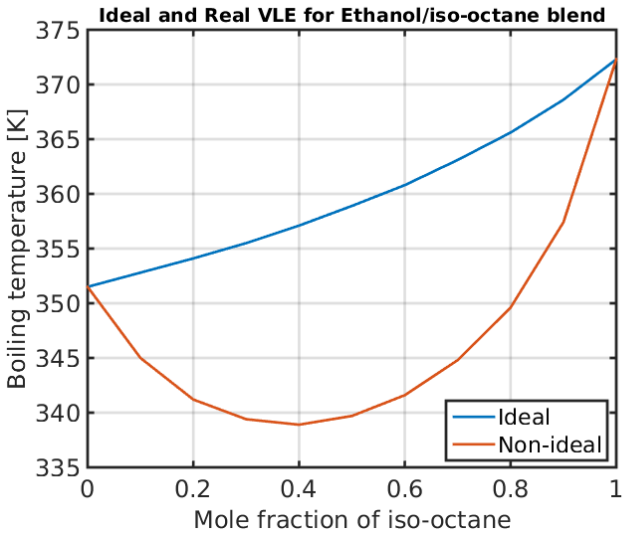

Figure 3.4: VLE of ethanol/iso-octane mixture at 1.013 bar ambient pressure.

The plot shows the boiling temperature of the mixture as a function of the mole fraction of iso-octane. Whereas the boiling temperature increases continuously with the blend's content of iso-octane in the ideal case, a different trend is observed in the non-ideal case. When the iso-octane content is low (and thus the ethanol content is high), the mixture's boiling point decreases as the mole fraction of iso-octane increases. However, when the iso-octane content is high, increasing the mole fraction of iso-octane raises the boiling point, as was observed when assuming ideal VLE. Similar trends were observed in an experimental study on VLE in binary ethanol/iso-octane mixture [71] in which blends with low iso-octane contents deviated strongly from ideal behavior. This indicates that the modified Raoult's law should be used when studying the evaporation of multicomponent mixtures containing polar compounds such as alcohols. This motivated an effort to implement non-ideal VLE in the VSB2 spray model to study the evaporation of multicomponent fuel blends. It should be noted that the minimum of the boiling temperature curve for the non-ideal case corresponds to the azeotropic mixture concentration for an ethanol/iso-octane blend (i.e. a blend with an iso-octane content of 40% by volume). The components of a blend with this composition cannot be separated by distillation. As mentioned previously, the mixture's behavior deviates strongly from ideality to the left of the azeotropic point.

Chapter 4

Results

This chapter introduces the spray submodels and solution algorithms used in the simulations. The most important results of the appended papers are then presented, together with the computational meshes and boundary conditions used in the corresponding studies.

All simulations were performed using OpenFOAM 2.2.x [65], [70]. Meshing was done using blockMesh, an OpenFOAM meshing tool based on hexahedral blocks.

4.1 Submodels used

The spray submodels used in the simulations are summarised in Table 4.1. Secondary breakup, mass and heat transfer were described using used relaxation equations (Chapter 3.2 (Eq. 3.13, 3.15). In short, a relaxation equation is a differential equation used to compute the rate of change of a physical quantity. The physical quantity is blob diameter in the breakup model, evaporated mass in the mass transfer model, and blob temperature in the heat transfer model. The secondary breakup time is calculated using the correlations of Pilch and Erdman [49]. Droplet velocity is calculated using the drag (momentum transfer) equation (Eq.3.17).

Solid cone sprays were examined in this work. Sprays of this type have a circular impact area at the base of the conical spray. The study of influence of droplet collisions was not in the scope of this work. In addition, no atomization model was used because the blob injection method was applied, under which the diameter of the injected blob is equal to the nozzle diameter. A unit injector was used. The injectors implemented in OpenFOAM differ mainly in the way in which velocity is calculated. For the unit injector, velocity is calculated from the input mass flow rate profile as shown in Eq 4.1

$$U = \frac{\dot{m}}{\rho C_D A} \tag{4.1}$$

Table 4.1: Submodels used.

Submodel	Name
Breakup	Pilch Erdman/Relaxation equation
Mass Transfer	Relaxation equation
Heat Transfer	Relaxation equation
Drag	Drag equation
Collision	None
Atomization	None
Type of spray	Solid cone
Injector (Injector setup)	Unit injector
Dispersion model	stochasticDispersionRAS

The droplets (contained in parcels) are injected in a disc centered on the position of the injector with a diameter equal to the nozzle diameter. The droplets' turbulent velocity is calculated using the stochasticDispersionRAS turbulent dispersion model. In the stochastic dispersion model [18], [45], the turbulent velocity is sampled from a Gaussian distribution (Eq. 2.9) with variance calculated from k and ϵ that are obtained from the turbulence model. The variance of the distribution is $\sqrt{\frac{2k}{3}}$. The turbulence model used is $k-\epsilon$ model with the coefficients tuned for the case under study.

To reduce grid dependency [16], the turbulent length scale (l_t) in the injection cell is fixed in the. This is done to ensure $l_t = L_{sgs}$, where L_{sgs} is set to the nozzle diameter. If l_t has to be equal to L_{sgs}, ϵ must satisfy Eq 4.2

$$\epsilon = C_\mu \frac{k^{\frac{3}{2}}}{L_{sgs}} \tag{4.2}$$

4.2 Solution algorithm used

The pressure velocity coupling in the non-linear Navier-Stokes equations was solved using the Pressure Implicit with Splitting Operators (PISO) method introduced by Issa [26]. The solution algorithm used in the solver (implemented in OpenFOAM) is summarized in Figure 4.1. The solver settings are used as input for the simulations. The input also specifies the use of the momentum predictor and the numbers of non-orthogonal correctors (nNonOrthCorr), and PISO loops (nCorr) to be used in the simulations. The momentum predictor can help stabilize solutions if needed because it generates better approximations for the velocity by solving for the velocity based on the pressure gradient. Correction for mesh non-orthogonality is done by specifying the number of non-orthogonal correctors (nNonOrthCorr), which causes the pressure equation to be solved the required number of times. The PISO loop is repeated nCorr times as specified in the input. A and H are matrices used to linearize the U equation to obtain the velocity solutions.

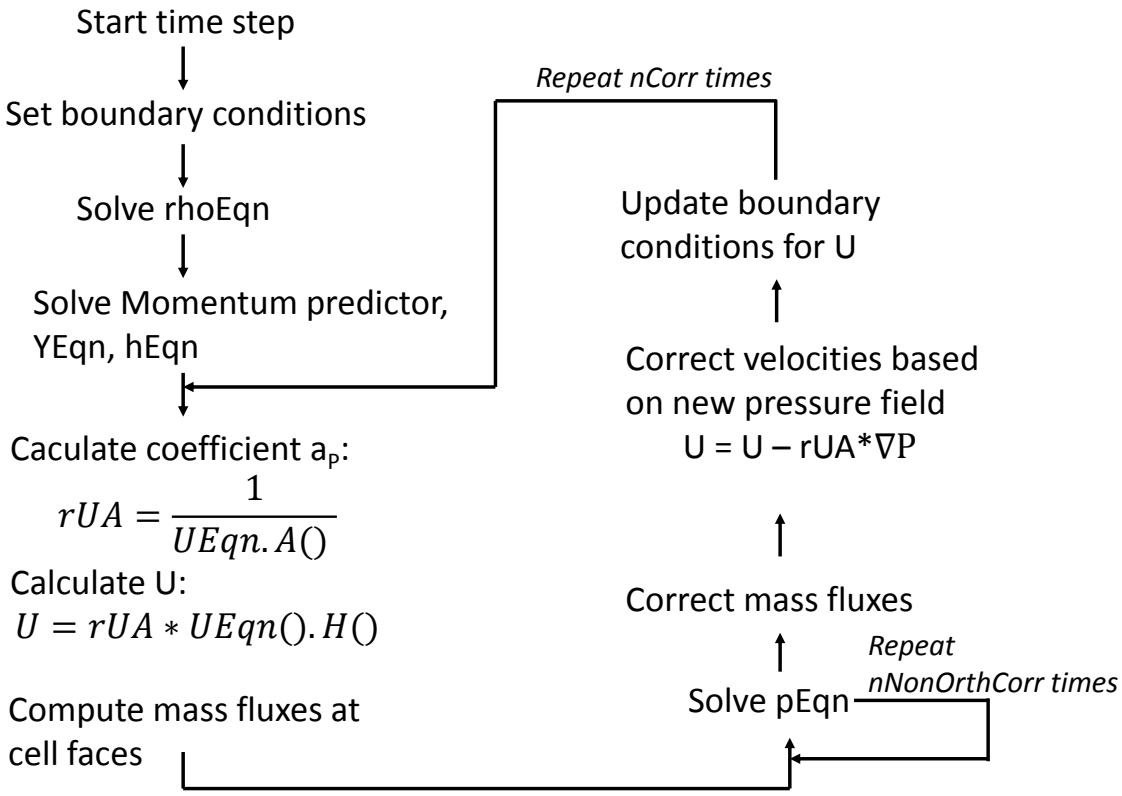

Figure 4.1: Solution algorithm.

In essence, the PISO loop uses the solutions generated by the momentum predictor to update the velocity boundary conditions. Before the PISO loop, the rhoEquation is solved for continuity, but the mass fluxes are corrected again in later steps. YEqn and hEqn are then used to solve for species and enthalpies, respectively. These equations are part of the solution algorithm but not the PSIO loop itself, which is used to solve the pressure-velocity coupling, as mentioned above. The PISO loop begins by solving the momentum equation using the momentum predictor, with the velocity being calculated from the previous pressure gradient. The updated velocity is then calculated (or corrected if the momentum predictor was used) from the coefficients A and H. In the following step, mass fluxes are computed and then the pEqn is solved for nNonOrthCorr times. Once the pEqn is solved, the mass fluxes are corrected and the velocity is corrected based on the new pressure gradients. In the final step of the PISO loop, the velocity boundary conditions are updated.

4.3 Modelling and validation of a two-component fuel spray, Paper I

The first paper deals with spray simulations for a two-component fuel consisting of n-Dodecane and iso-Octane, which are surrogates for diesel and gasoline, respectively.

4.3.1 Boundary conditions

The boundary conditions were the same as in the experiment performed by Zheng et al [75] and the simulations' results were compared to the experimental data reported by those authors. The boundary conditions for the baseline experimental case are presented in Table 4.2.

Table 4.2: Boundary conditions.

Ambient temperature	830 K
Ambient pressure	40 bar
Injection pressure	800 bar
Injection duration	5.6 ms
Total injected mass	24.65 mg
Nozzle diameter	168 μm
Fuel	2 component surrogate

Fuel composition Four cases were studied in the experiment and the simulations. The first was pure diesel (assigned the label G0; n-Dodecane was used as a diesel surrogate in the simulations). The remaining 3 were gasoline-diesel blends (GDB) containing 20%, 40% and 60% gasoline (iso-Octane in the simulations) by volume. These blends were assigned the labels G20, G40, and G60, respectively.

4.3.2 Computational mesh

Simulations were performed using a 3-D grid representing the geometry of a constant volume combustion chamber. The length of the smallest cell along the spray axis (negative z-axis) axis was 1mm. Top and full cylinder views of the mesh are shown in Figure 4.2. The injection location is in the middle of the refined square region, and the injection was directed downwards (in the negative direction of the z-axis). The simulation's input settings are shown in Table 4.3.

Table 4.3: Input settings for simulation.

Number of blobs	10^5
Time step	10^{-6} s
Courant number	0.5
Grid size along injector axis	1 mm

4.3.3 Summary of results

Some important results from this study are highlighted here. For further results and discussion, the reader can refer to Paper I.

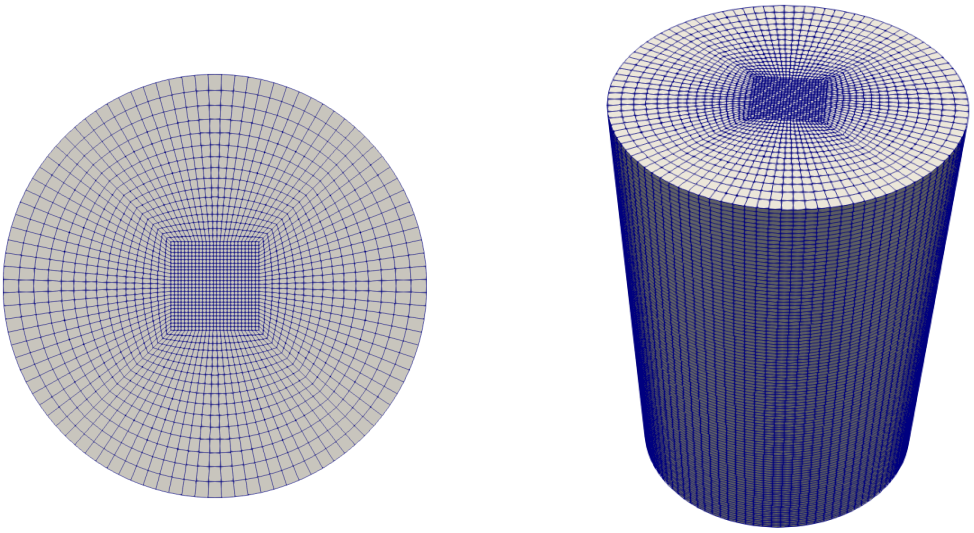

Figure 4.2: Top and full cylinder views of mesh.

For the simulations, n-Dodecane was used as surrogate diesel and iso-Octane was used as surrogate gasoline. Both are commonly used surrogate fuels in fuel spray studies. n-Dodecane has a greater molecular weight (170 g/mol) than iso-octane (114 g/mol) and accordingly also has a higher heat of vaporization (55.6 kJ/mol as compared to 31.5 kJ/mol). The predicted liquid and vapor penetrations for each studied case are compared to the corresponding experimental data in Figure 4.3. The

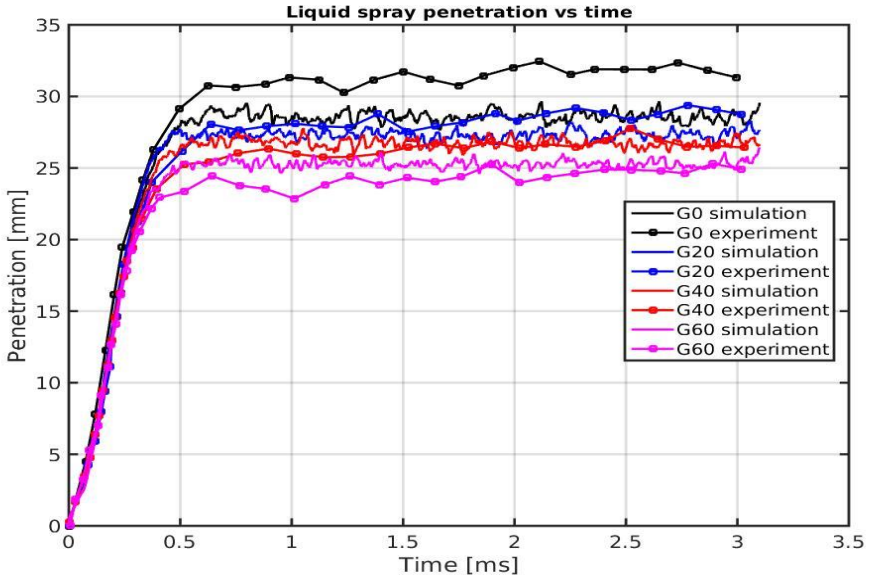

Figure 4.3: Liquid penetration vs. time.

liquid penetration clearly decreases as the content of gasoline (iso- octane) increases on going from G0 to G60. This is expected because iso-Octane, being the lighter component, is more volatile and evaporates faster than n-Dodecane. The difference between the experimental and simulated liquid penetration is 7.5% for G0 and below 5% for all other cases. The comparatively large difference seen for G0 may be because the properties of the diesel surrogate n-Dodecane differ more from those of real diesel fuel than the properties of n-octane (the gasoline surrogate) differ from those of real gasoline. Overall, however, the experimentally observed trends are well reproduced by the simulations.

The individual evaporation rates for the two components are shown in Figure 4.4 for the G20 case. It is clear that iso-Octane is the more volatile of the two

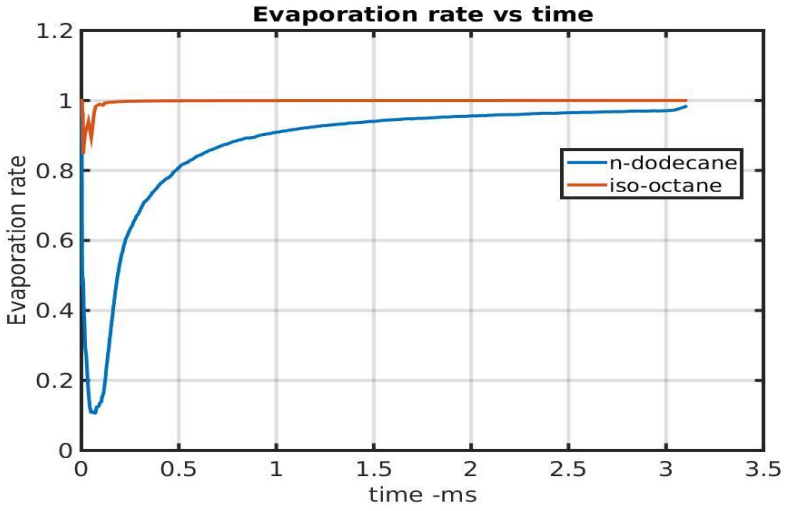

Figure 4.4: Evaporation rates of the two components of the G20 blend over time.

components and therefore has a much higher evaporation rate.

Each component also has different spatial distribution of its vapor. The distribution of the vapor mass fraction along the spray axis is shown in Figure4.5 along with a contour plot showing the two-dimensional distribution of the vapor of both components for the G20 case. The vapor mass fraction of the more volatile component, iso-Octane, peaks closer to the injector. The peak vapor mass fraction for n-Dodecane is higher than that for iso-Octane because n-Dodecane comprises 80% of the G20 blend by volume.

Conclusion A method for solving the coupled non-linear equations governing multicomponent evaporation is implemented and the spray model predictions are

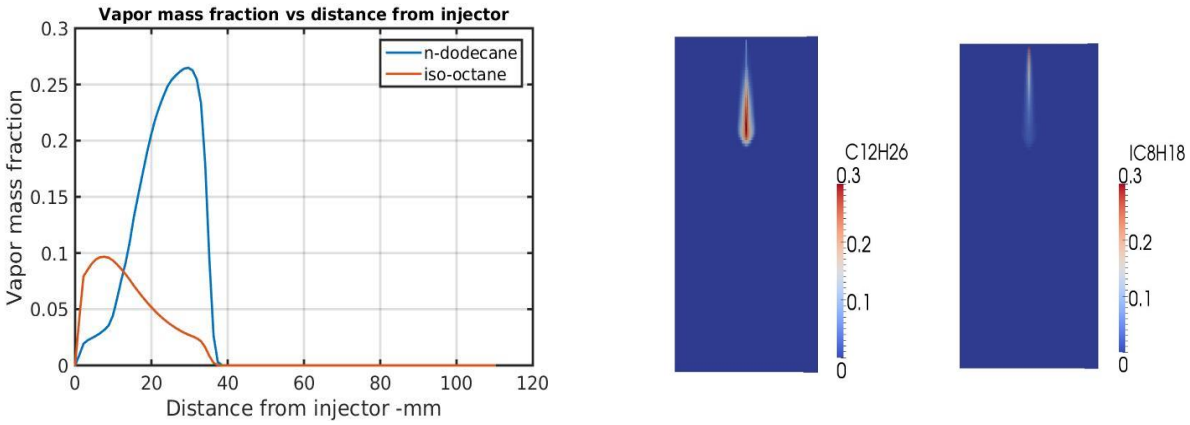

Figure 4.5: Left: Axial distribution of individual vapor mass fraction, right:Contour plot of individual vapor mass fractions.

validated against experimental liquid prediction. The following conclusions can be drawn:

- Liquid penetration results were compared with experimental data. A decreasing trend was seen with increasing iso-Octane content as observed in the experiment. The difference in liquid penetration id around 7.5% for G0 case and it is less than 5% for all the other case. A similar decreasing trend was seen for vapor penetration.
- A clear difference in vapor distribution between the components could be captured.
- Differential evaporation was seen to decrease with increase in gas temperature. Details about this can be seen in Paper I.

Overall it can be concluded that the new method implemented for calculating multicomponent evaporation can be recommended as an alternative to the previously existing method. The method can easily be scaled to handle a larger number of fuel components.

4.4 Influence of non-ideal Vapor Liquid Equilibrium, Paper II

The second paper investigated the importance of considering non-ideal vapor liquid equilibrium. Its most important results are summarized below; for a more detailed

discussion, the reader is referred to Paper II. This study focused on the influence of non-ideal thermodynamics for a two-component spray consisting of Ethanol and iso-Octane in a constant volume combustion vessel.

4.4.1 Boundary conditions

The simulations were compared to experimental data obtained by [37], which were previously used in [35]. The conditions mimic an intermediate load operating point of direct injection gasoline engines. The boundary conditions set up in the experiment and used in the simulation are summarized in Table 4.4

Table 4.4: Boundary conditions.

Ambient temperature	473 K
Ambient pressure	5.6 bar
Injection pressure	200 bar
Injection duration	1 ms
Total injected mass	16 mg
Nozzle diameter	200 μm
Fuel	2 component

The experiments were performed in a constant volume combustion vessel with a 6- hole injector through which the total mass of fuel was injected. Conversely, the simulations were performed for a single hole injector to focus the study on a single spray. The internal gas flow through the chamber had a velocity 3-10 cm/s is negligible when compared to the liquid jet velocity of around 100m/s. The liquid penetration was measured by shadowgraphy and vapor penetration was measured by the by Schlieren imaging technique.

Fuels used The fuel mixtures used in the experiment were gasoline (E0), ethanol (E100), and blends with varying amounts of each of the fuel components.

4.4.2 Computational setup

The mesh used for this study was the same as that shown in Figure 4.2. The input parameters used in the simulation are the same as in Table 4.3. Iso- octane was used as a surrogate for gasoline (E0) in the simulations. Gasoline is a mixture of several compounds and the exact composition of a given batch of gasoline is typically not known. Iso-octane is therefore often used as a gasoline surrogate with known physicochemical properties. A uniform mass flow rate profile was used. Opening and closing transients are ignored because of the absence of experimental mass flow rate profile data. This would be expected to give rise to some differences between the experimental results and the simulation. Four different fuel blends were simulated: E0, E10, E40 and E100. For each blend, the number indicates the content of ethanol as a percentage by volume.

4.4.3 Properties of fuels

iso-Octane is the more volatile of the two components: its enthalpy of vaporization (282.2 KJ/Kg) is much lower than that of ethanol (852.3 KJ/Kg).

4.4.4 Summary of results

As mentioned earlier, the saturated vapor mass fraction is given by Eq. 4.3

$$y_{fu,eq,i} = \frac{M_{fu,i}}{M_{mix}} \frac{P_{sat,i}(T_{bub})}{P} X_{i,l}\gamma_i \tag{4.3}$$

If ideal thermodynamics is assumed, the activity coefficient γ_i is unity because interactions between different types of molecules (i.e. ethanol and isooctane) are disregarded. When applying non-ideal thermodynamics, the activity coefficient is calculated for each type of fuel molecule using Eq. 3.34 as discussed in Chapter 3.3. The calculated VLE for various ethanol/iso-octane blends at 1 bar ambient pressure is shown in Figure 4.6.

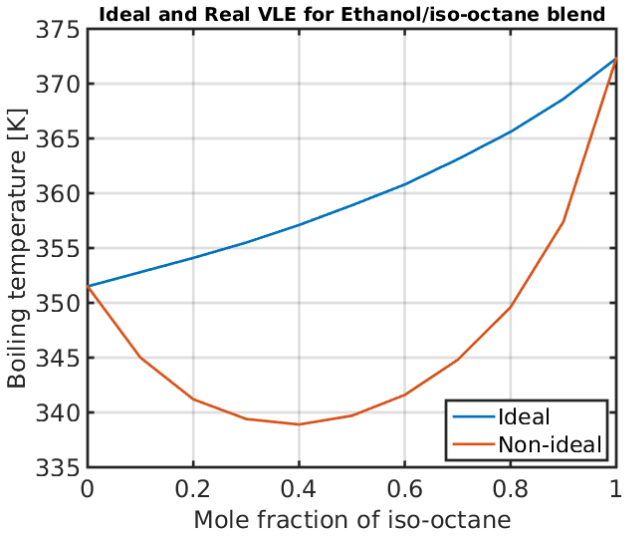

Figure 4.6: VLE of ethanol/iso-octane mixture at 1.013 bar ambient pressure.

The boiling temperature deviates strongly from the ideal curve when the assumption of ideality is removed. This prompted a deeper investigation into the effects of non-ideal VLE on the results of CFD simulations of fuel sprays. The influence of non-ideal VLE was studied using two fuel blends: E10 and E85. Experimental data was available only for E10. The experimental liquid and vapor penetration for E10 are shown in Figure 4.7 together with the simulated results obtained under the assumption of ideal and non-ideal spray behavior.

The liquid and vapor penetration under the assumption of ideality did not differ greatly from those under the assumption of non-ideality in the E10 case, but more pronounced differences were observed for the E85 case (Figure 4.8). Interestingly, the difference for the liquid penetration was more pronounced than that for the

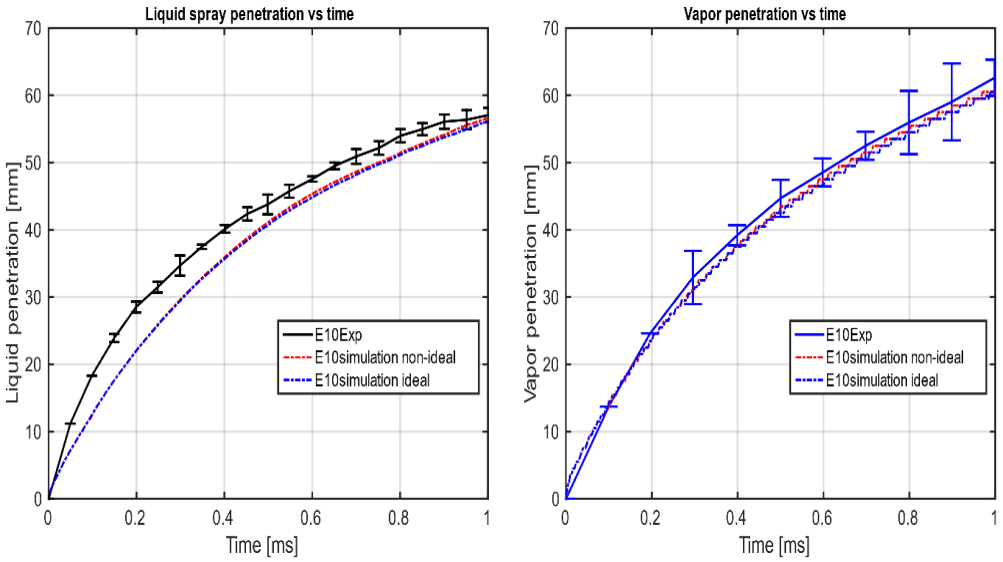

Figure 4.7: Liquid and vapor penetration vs. time for E10 case.

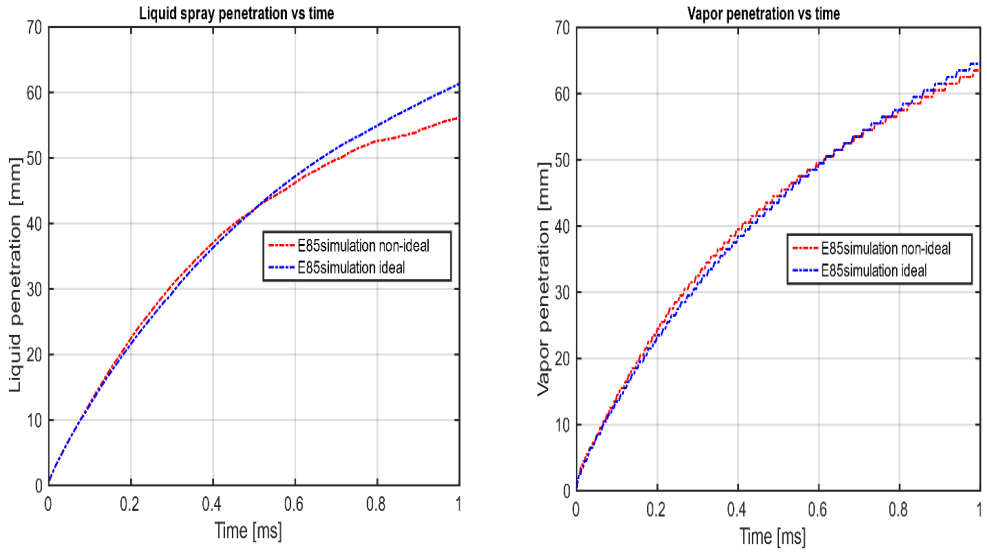

Figure 4.8: Liquid and vapor penetration vs. time for E85 case.

vapor penetration. To understand why the assumption of non-ideal VLE affected the liquid penetration more severely in the E85 case, the radial fuel distribution for each of the component is plotted for the E10 and E85 cases (see Figure 4.9). For E10, the distributions for both fuel components under the ideal and non-ideal cases are quite similar. However, the difference is quite pronounced in the E85 case. This is consistent with the general finding that blends with higher alcohol contents exhibit greater deviations from ideal behavior because intermolecular interactions become stronger and more important as the content of polar molecules increases. Additionally, both the liquid penetration curves and the radial vapor distribution

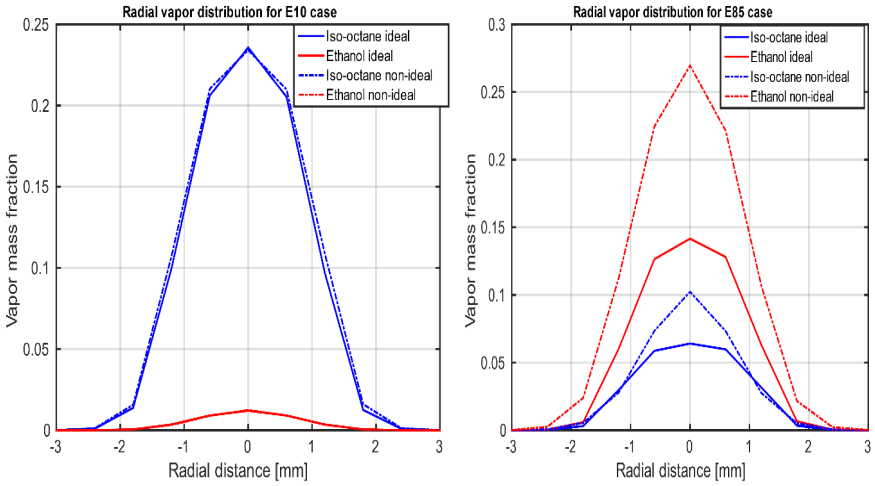

Figure 4.9: Radial distribution of vapor mass fractions for E10 and E85 case.

show that the rate of evaporation for E85 is predicted to be higher in the non-ideal case.

Conclusion Overall, these results indicate that the assumption of ideal VLE based on Raoult's law does not accurately capture fuel spray behavior in the studied cases. The impact on liquid and vapor penetrations seems relatively small, but clear differences are revealed upon further analysis of spray structure. These observations also suggest that the influence of ethanol molecules on iso-octane is stronger than vice versa. Similar findings have been reported previously [6].

4.5 Influence of resolving injector orifice and creating child parcels, Paper III

Many studies have focused on resolving the region near the orifice where the spray is dense. Some examples with important conclusions are now summarized. [38] studied 3 grid sizes (coarse to fine relative to orifice diameter) and it was shown that shown that grid cells with the size of at least the order of the orifice diameter were required to achieve a reasonable agreement with experiment for liquid, vapor penetrations and axial gas velocity. But grid study was limited to liquid and vapor penetrations. [4] Performed grid study for spray G conditions for grid size with smallest grid size for the fine mesh being 125 μm (orifice: 165 μm). The fine mesh showed good agreement with experimental liquid penetration but the analysis was again limited to liquid penetration and additionally SMD. Apart from studying the influence of resolving near orifice region, it is also important to study the resolution of the injector orifice itself. [2] has shown that at least two cells (across the injector orifice) are required to accurately predict a gas jet. Spray simulations were not done in [2] but suggested that the implications could indeed be extended for sprays. [63]

Table 4.5: Boundary conditions.

Ambient temperature	900 K
Ambient pressure	60.5 bar
Injection pressure	1500 bar
Injection duration	1.5 ms
Total injected mass	3.46 mg
Nozzle diameter	84 μm

concluded that beyond a certain grid size (two times orifice diameter), the accuracy of predicting sprays converges (w.r.t liquid and vapor penetration) and resolving the grid cells further does not produce any further significant difference. Cases were studied from unresolved up to 4 cells resolving the orifice. However the analysis was mainly confined to liquid and vapor penetrations. To date, few studies have examined the influence of resolving the injector orifice on detailed predictions of spray behavior under high pressure and temperature diesel engine conditions. The study presented below was therefore conducted to address this knowledge gap. The injector orifice was resolved into 9 cells and the mesh was modified accordingly to accommodate a gradual increase in grid cell size from the core of the spray to the periphery of the cylinder. The main results of this study are summarized below; for further details, the reader is referred to Paper III.

4.5.1 Boundary conditions

All simulations were compared to experimental data on ECN spray A from the Sandia national laboratory [12] for non-combusting conditions. The boundary conditions are summarized in Table 4.5

4.5.2 Computational mesh

A constant volume cylindrical combustion chamber was meshed using blockMesh (Figure 4.10). Two mesh setups were studied: one where the injection orifice was not resolved (i.e. where the cell size in the x and y direction were of the order of the injector orifice diameter) and another where the orifice was resolved into 9 cells. Top views of both the meshes is shown in Figure 4.11. The Figure is zoomed to same level for both the meshes in order show the injector orifice region.

Both the meshes were refined in the spray region where there is extensive spray-gas interactions, but not in the periphery as the gas there is under more or less at ambient conditions. The nozzle orifice diameter was $84\mu m$. In the unresolved mesh, each cell in the refined region had dimensions of 125x125x250 μm. Each cell in the x-y plane was thus comparable in size to the nozzle orifice diameter, albeit slightly coarser. In the resolved mesh, the injector orifice was resolved into 9 cells, with 3 cells spanning the diameter. The innermost cell in the core spray region (within the orifice) had dimensions of 28x28x62.5 μm.

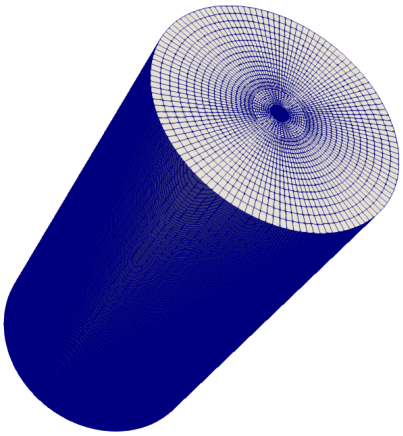

Figure 4.10: Constant volume chamber mesh.

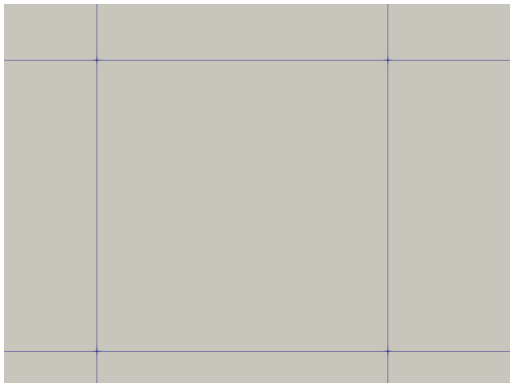

(a) Unresolved orifice

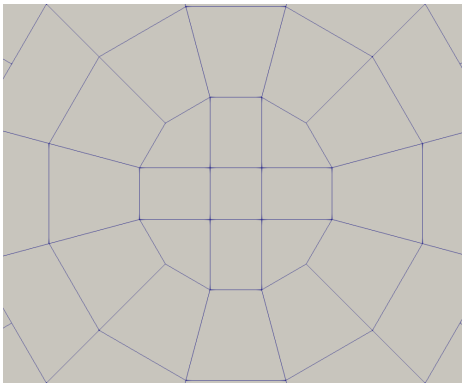

(b) Resolved orifice

Figure 4.11: Top view of the unresolved and resolved meshes.

4.5.3 Grid convergence study

A grid convergence study was undertaken to verify the solution method used. The aim of this study was:

- To calculate extrapolated values for the chosen fields of interest: The extrapolated values represent a grid finer than the finest mesh used in the study. The extrapolated values are then compared against the predictions of the existing mesh.
- To calculate Grid Convergence Index (GCI): GCI is used to judge the uncertainty of the solution method. It represents 95% confidence interval.

These extrapolated values and GCI can be used to judge if it is sufficient to resolve the injector orifice into 9 grid cells and what is the uncertainty level associated with this assumption.
The study involves following a five-step procedure as suggested by ASME V&V 20-2009 standard [5]. The procedure is used to calculate extrapolated values and the

extrpolated uncertainty estimates (using the Richardson Extrapolation (RE) method [59]) for the variables under study. GCI is then calculated by multiplying the RE error with a factor of safety F_s.
Three meshes are used for this study. The three are geometrically similar meshes (which is suggested to get accurate results for this procedure). Mesh 1 (Figure 4.12a): Injector orifice is resolved into 9 cells, the innermost cell surrounding the orifice is 28 μm in the x and y directions. Mesh 2 (Figure 4.12b): Injector orifice is unresolved and the innermost cell is 125 μm which is of the order of the orifice diameter, Mesh 3 (Figure 4.12c): Injector orifice is unresolved and the innermost cell is 250 μm which is larger than the orifice diameter. Top view of the three meshes in Figure 4.12 are zoomed (to the same level) to show the injector. The red squares indicate the grid celsl surrounding the orifice which are also the grid cells with minimum length in the x and y directions. A representative grid size h is chosen for each of the mesh. In

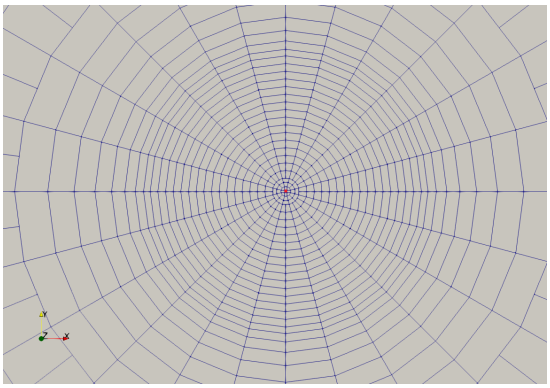

(a) Resolved orifice, min grid size = 28 μm

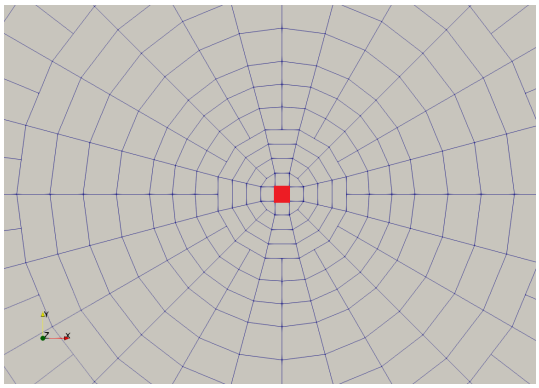

(b) Unresolved orifice, min grid size = 125 μm

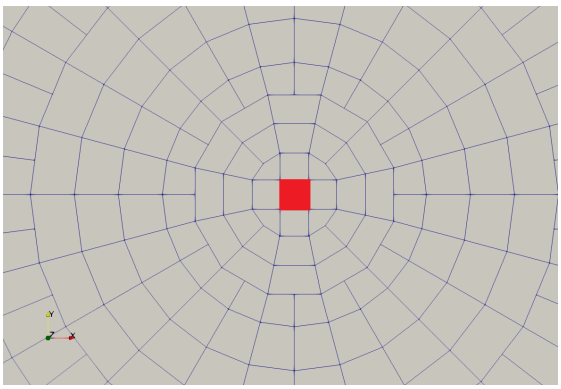

(c) Unresolved orifice, min grid size = 250 μm

Figure 4.12: Top view of the unresolved and resolved meshes with cylindrical core.

this case, h is the size of the grid cell surrounding the orifice, such that $h1 < h2 < h3$ and $r21 = h2/h1$, $r32 = h3/h2$. $\varepsilon_{ij} = \phi_j - \phi_i$ and ϕ_i is the simulation value of the variable under interest on the i^{th} mesh.

The extrapolated values of the variables are calculated using Eq. 4.4

$$\phi_{ext}^{21} = (r_{21}^{p}\phi_1 - \phi_2)/(r_{21}^{p} - 1) \tag{4.4}$$

where p is the apparent order of the method. Details of how p is calculated can be found in Paper III (Section 5, Eq. 30-32). Finally the Grid Convergence Index (GCI) is given by Eq. 4.5

$$GCI^{21}_{fine} = \frac{F_s e^{21}_a}{r^p_{21} - 1} \tag{4.5}$$

F_s is factor of safety and $F_s = 1.25$ (ASME, 2009, 2-4.1). Using this value of F_s would result in a GCI with 95% confidence interval. The variables under study, extrapolated values, extrapolated errors, and GCI are given in Table 4.6 .

Table 4.6: Uncertainty analysis.

	Vapor penetration (1.4ms ASOI)	Uax (25mm)	Z (25mm)
h1	$28\mu m$	$28\mu m$	$28\mu m$
h2	$125\mu m$	$125\mu m$	$125\mu m$
h3	$250\mu m$	$250\mu m$	$250\mu m$
r21	4.46	4.46	4.46
r32	2	2	2
ϕ_1	52.38	72.24	0.113
ϕ_2	54.54	77.23	0.119
ϕ_3	56.41	84.9	0.134
ϕ^{21}_{ext}	50.91	71.23	0.112
e^{21}_{ext}	2.91%	1.42%	0.65%
GCI^{21}_{fine}	3.53%	1.75%	0.81%

The plot of the key variables under consideration for the three grids is shown in Figure 4.13. The extrapolated values are shown with blue dots. Liquid penetration could not be used for uncertainty analysis as the values for unresolved (0.125 mm) and resolved meshes were very close to each other. The simulations showed that there is a relatively more clear trend due to grid refinement for vapor penetration. However, liquid penetration is also shown here for reference.

The extrapolated value (represented by a blue dot at t=1.4ms) for vapor penetration is a bit lower than the finest grid but it is seen that for axial velocity and mixture fraction, the extrapolated values are close to the values for the finest grid resolution used which suggests that the finest grid resolution is reasonably sufficient for the purpose of this study.

4.5.4 Summary of results

The following sections present the main results of studies on the influence of resolving the injector orifice and the influence of resolving stripped off droplets.

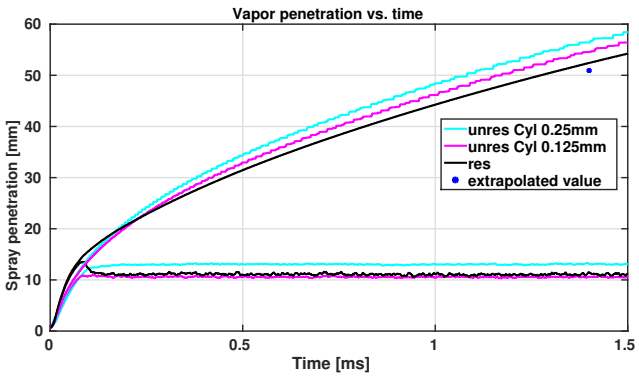

(a) Vapor penetration

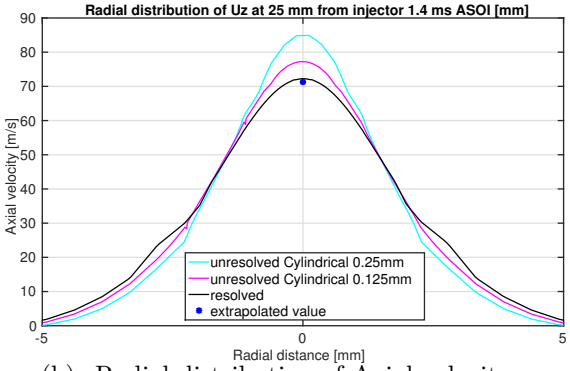

(b) Radial distribution of Axial velocity

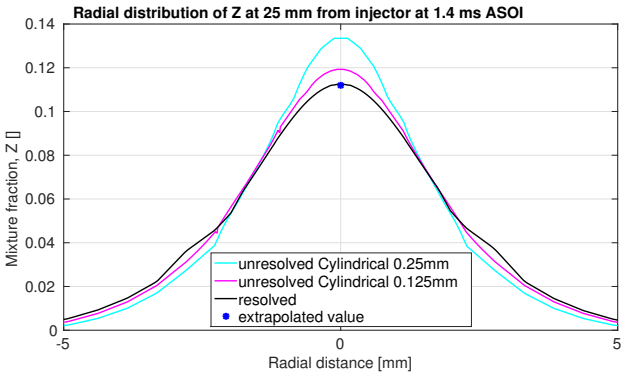

(c) Radial distribution of mixture fraction

Figure 4.13: Grid convergence of key variables.

Influence of resolving the injector orifice Two meshes were considered (as shown in Figure 4.11): one that resolved the orifice and one that did not. As shown in Figure 4.14, the liquid and vapor penetration predicted using the resolved mesh were both higher than the corresponding values predicted with the unresolved mesh. This difference can be explained by comparing the evaporation rates for the two meshes. The evaporation rate was defined as the ratio of the evaporated liquid mass to the injected liquid mass and is plotted for both meshes as a function of time in Figure 4.15.

Although the difference is small, the expanded plot clearly shows that the rate of evaporation for the resolved mesh is lower. This may be because the gas in the smaller grid cells become saturated more quickly than in the larger grid cells of the unresolved mesh. Therefore, the evaporation rate is lower and the liquid penetration is higher with the resolved mesh. Another possible reason is that (as explained in Section 5.0.1 of Paper III), there is more numerical diffusion in the radial direction when using the unresolved mesh due to the Cartesian core.
The axial and radial mixture fractions of the two meshes are plotted together with the values observed experimentally at 1.4 ms ASOI in Figure 4.16) .

Both the unresolved and resolved meshes yielded reasonably good agreement with experiment, especially for the axial profile. However, the axial profiles for the two

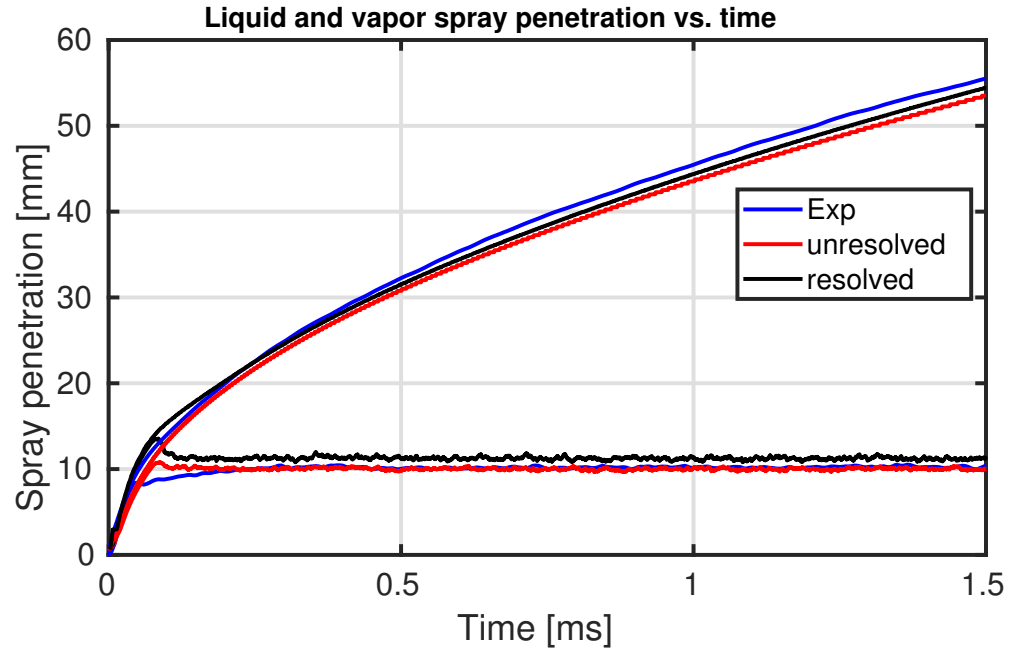

Figure 4.14: Liquid and vapor penetration predicted with the resolved and unresolved meshes, and the corresponding experimental values.

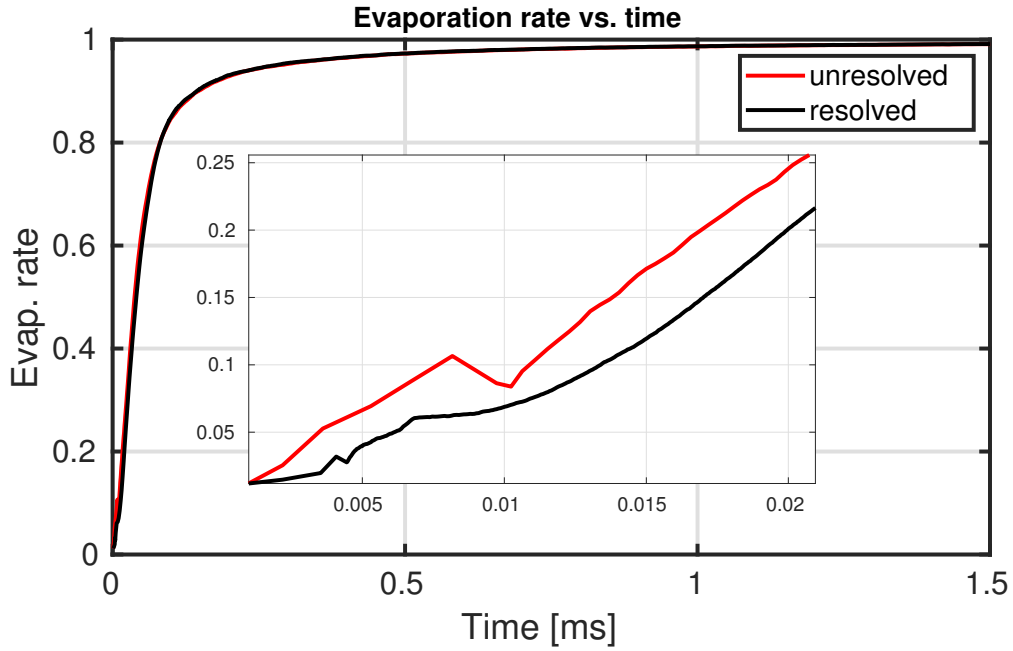

Figure 4.15: Evaporation rate predicted with the resolved and unresolved meshes.

meshes differed close to the injector. Experimental data was not available for the near nozzle region, so it was not possible to validate the predictions in this region. It is possible that the value of the axial mixture fraction close to the injector is higher with the resolved mesh because of the smaller grid cells, which become saturated more quickly than those of the unresolved mesh. Another possible reason is that

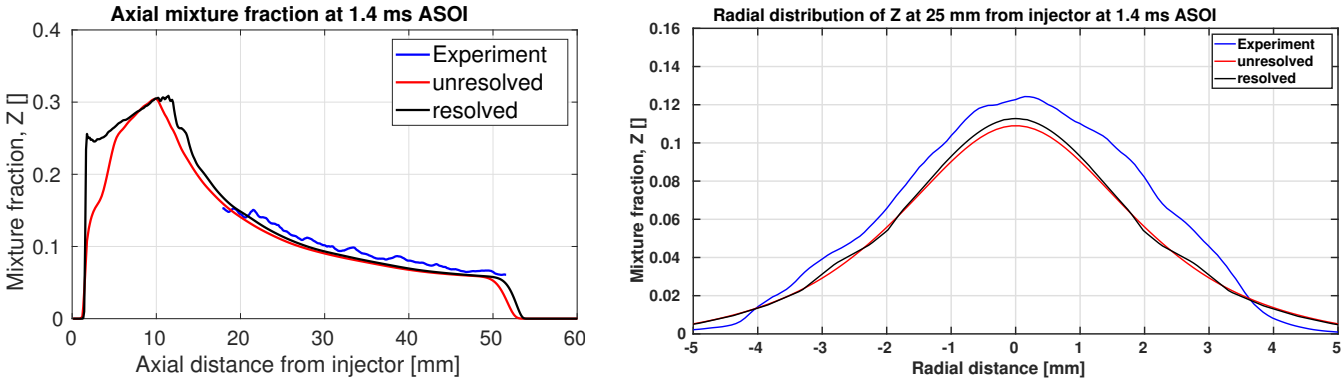

(a) Axial profile

(b) Radial profile

Figure 4.16: Mixture fraction profiles at 1.4ms ASOI.

there is more diffusion in the radial direction with the unresolved mesh due to the Cartesian core.
Although the results for the radial mixture fraction agreed reasonably well with experiment, there was a slight difference in the peak values. The peak for the resolved mesh is slightly higher and closer to the experimental peak for the reasons mentioned previously. Similar trends were also observed for the axial and radial gas velocity distributions. For details of these results, the reader is referred to Paper III (Chapter 6.1.4).

Influence of creating stripped of child blobs The stripped off mass is defined as the liquid mass removed by secondary breakup (Section 3.2.4). Two cases were simulated using the ECN spray A conditions specified in Table 4.5: one case where the stripped off mass was used to create new child blob (if its mass was greater than 1% of the mass of the original parent blob) and another where the stripped off mass was not used to create new child blob and was instead retained as a mass package in the original blob (each blob is divided into 10 mass packages, see Section 3.2.3). Inspiration for this study was drawn from the work performed by Karlsson, Chapter 6.1.7 in [30], where the idea of creating stripped off child parcels was first introduced (and studied for a different operating condition). The reason for studying this is as follows. The smaller stripped off droplets in the liquid blob transfer the same momentum as the bigger droplets. Creating new blobs from stripped off droplets is thus more accurate in terms of momentum transfer. However, it is not clear how much of a difference this makes under the high pressure and temperature conditions of diesel sprays. The two simulation cases were compared using the resolved and unresolved meshes; the resulting liquid and vapor penetration curves are shown in Figure 4.17. When using the unresolved mesh, there is a noticeable difference in liquid penetration between the stripped and non-stripped cases; this difference disappears when using the resolved mesh. The difference between the meshes occurs because the finer mesh of the resolved orifice increases momentum transfer to the gas. As a result, the gas velocity is increased and the difference in velocity between the gas and the droplets is reduced, which in turn reduces the extent of stripping

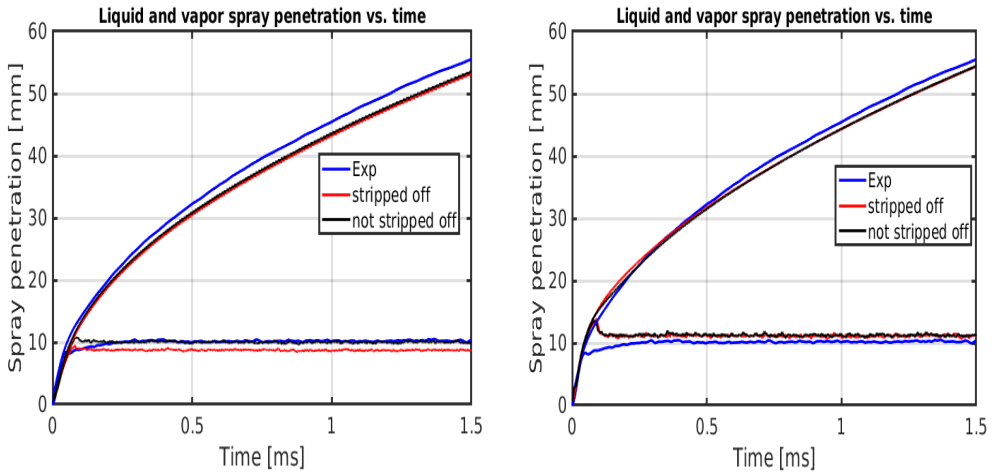

Figure 4.17: Liquid and vapor penetration with and without stripping off child blobs, Left:unresolved orifice. Right:resolved orifice.

off . This finding is supported by the Sauter Mean Diameter (SMD) plots for the two cases (Figure 4.18). The SMD is the diameter of a representative droplet whose surface area to volume ratio is equal to the ratio of the sum of all the droplet volumes in the spray to the sum of all droplet surface areas. The difference is less pronounced

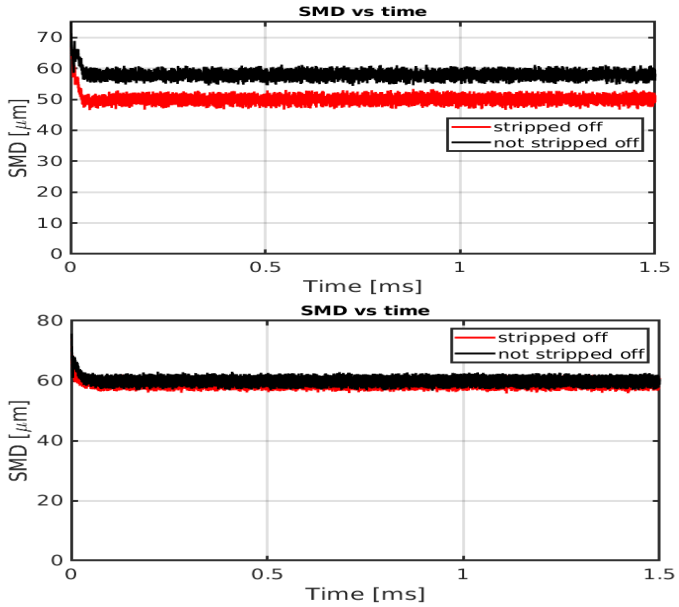

Figure 4.18: SMD vs. time for the two meshes with and without stripping off, Top: unresolved, Bottom: resolved.

for the resolved mesh, confirming that less stripping occurs.

Conclusion

- The liquid and vapor penetration values predicted by the resolved mesh were

slightly higher than those of the unresolved mesh. The resolved mesh predicted a lower evaporation rate as the fine grid cells were saturated relatively quicker.

- Turbulence (measured by k and ϵ) and mixing rate of fuel were higher for the resolved mesh especially in the fuel rich region. These results can be found in PeperIII. The mixing rate is an important parameter to consider when studying combustion.

Overall it can be concluded that only looking at the liquid and vapor penetrations the difference might be small between the two meshes. But further investigation (e.g. radial mixture fraction and velocity profiles close to the injector, turbulence and mixing rates) reveals a clearer difference between the two meshes. It is worthwhile to study the influence of the two meshes for combusting sprays.
As for the influence of creating new stripped off child blobs, the following conclusion was drawn:

- Under high pressure and temperature diesel engine like operating conditions, the formation of new child blobs from stripped off mass, has no significant effect on spray predictions.

The influence of introducing bubble was also studied and it was seen that introducing the bubble resulted in a more controlled evaporation. For further details on these conclusions the reader is suggested to refer to PaperIII.

4.6 Modelling a three-component spray and studying the influence of resolving the counterbore of a GDI injector, Paper IV

The final study focused on simulations of ECN spray G [13]. This case, which was designated G1 E00, involves a three-component surrogate fuel that is used to represent gasoline (G1 refers to the operating conditions and E00 refers to the multicomponent case). The fuel is injected using a Gasoline Direct Injection (GDI) injector into a constant volume combustion chamber under gasoline engine pre-combustion conditions.

4.7 Boundary conditions

The G1 operating conditions were chosen for validation. The G1 boundary conditions are summarized in Table 4.7.

The three-component fuel consisted of n-Pentane (36 % by volume), iso-Octane (46 % by volume) and n-Undecane (18 % by volume). An 8-hole counterbore injector with an orifice diameter of 165 μm and a counterbore step diameter of 388 μm was used

Table 4.7: Boundary conditions spray G.

Ambient temperature	573 K
Ambient pressure	6 bar
Injection pressure	200 bar
Injection duration	0.78 ms
Total injected mass	1.25 mg
Nozzle diameter	780 μm
Fuel	3 component

in the reference experiments. Liquid properties of the fuel used for the simulations are obtained from equations using National Standard Reference Data Series [44] and VDI functions [67]. The simulations were performed for two purposes: to study the influence of resolving the counterbore and validate the treatment of multicomponent evaporation.

4.8 Computational mesh

A constant volume combustion chamber was meshed using blockMesh. A reduced volume ($\frac{1}{8}$ th) of the original chamber volume was meshed because the focus was on a single spray. The spray was injected vertically downwards (in the negative direction along the z-axis). Two meshes were used in the simulations: counterbore resolved and counterbore un- resolved. The constant volume chamber and a top view of the mesh with the counterbore are shown in Figure 4.19

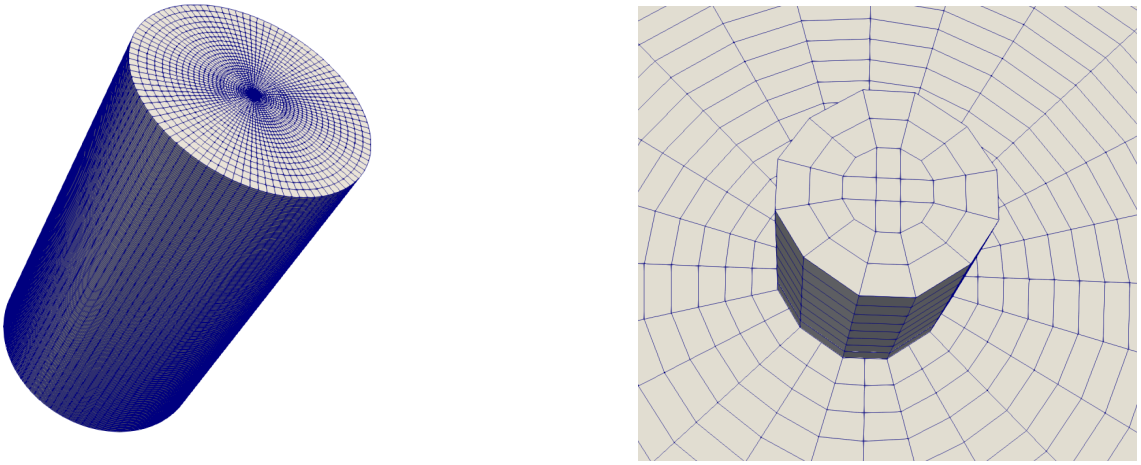

Figure 4.19: Left: 3D view of the mesh. Right: Top view of the mesh with the counterbore.

4.9 Summary of results

The liquid and vapor penetration for the two meshes is shown in Figure 4.20.

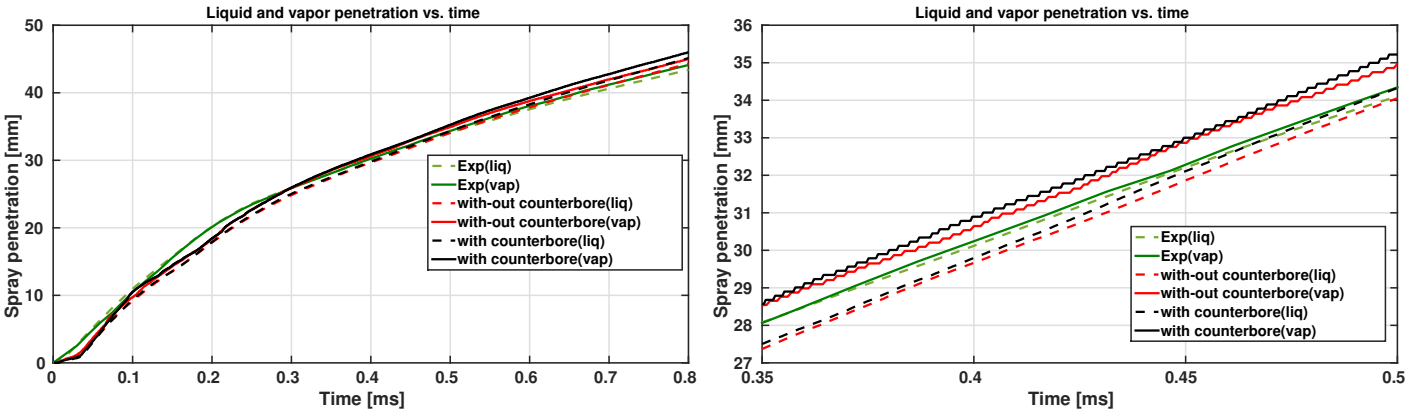

Figure 4.20: Liquid and vapor penetration vs. time (zoomed around 0.4ms in the 2nd subfigure).

In the simulations, the spray axis is the same as the injector axis, the spray is injected vertically downwards. The aim in the simulations was to focus on a single spray. It should be noted that in the experiment however, each spray was injected at an angle from the injector axis. The angle between the injector and spray axis in the experiment was 37°. The experimental penetration lengths were measured along the injector axis and this was corrected here, to get the penetration lengths along the spray axis to keep the comparison with the simulations consistent.
Both meshes achieved reasonable agreement with experiment, and the differences between their predictions were small. The difference in liquid penetration did not exceed 1.84%. Nevertheless, the expanded plot on the right of Figure 4.20 shows that the difference in penetration lengths (especially liquid penetration length) increased from around 0.4 ms onwards, and that the mesh with the counterbore predicted a higher liquid and vapor penetration. A probable reason for this is that the extent of fuel-air mixing for the mesh with the counterbore resolved, was greater causing the gas velocity to increase and reducing the relative velocity of the liquid jet and its drag, which would tend to lengthen the liquid core when compared to the mesh without the resolved counterbore. It was also seen that the mesh with the counterbore predicted larger droplets than the mesh without the counterbore. For results showing the lagrangian spray and droplet size distribution, the reader is referred to PaperIV.

There was a clear fuel-air mixing seen in the counterbore region for the mesh with resolved counterbore as shown by superimposing a plot of the velocity vectors on a contour plot of the total fuel fraction in gas (Figure 4.21). The mixing of fuel and air can be quantified in terms of the mixing rate, i.e. the mass weighted average of $\frac{\epsilon}{k}$. The mixing rates for the two meshes are shown in Figure 4.22 ; the rate is clearly higher for the mesh with the counterbore, especially in the counterbore region but also in the spray region.

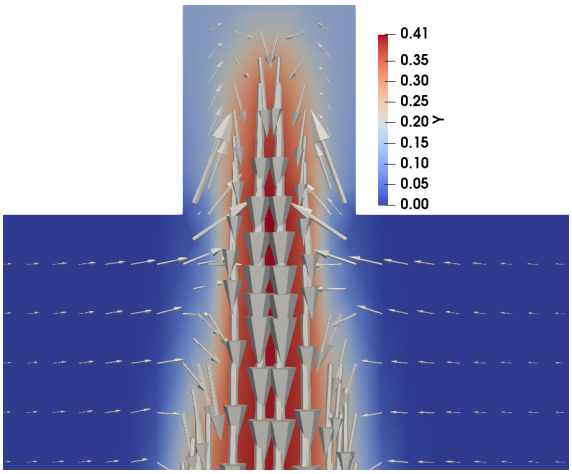

Figure 4.21: Velocity vector plot for the mesh with resolved counterbore.

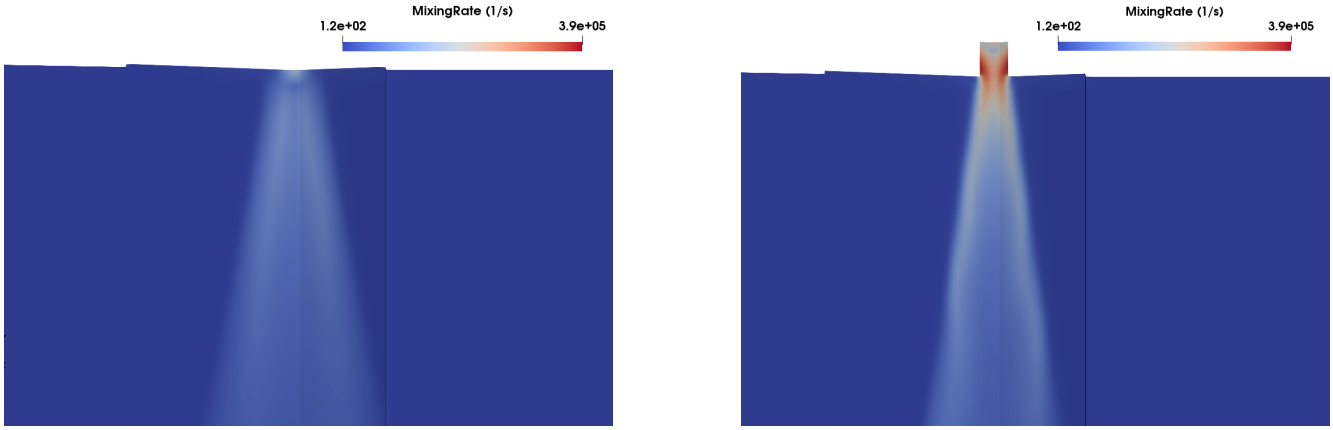

(a) with-out counterbore (b) with counterbore

Figure 4.22: Contour plots of the mixing rate with and without the counterbore.

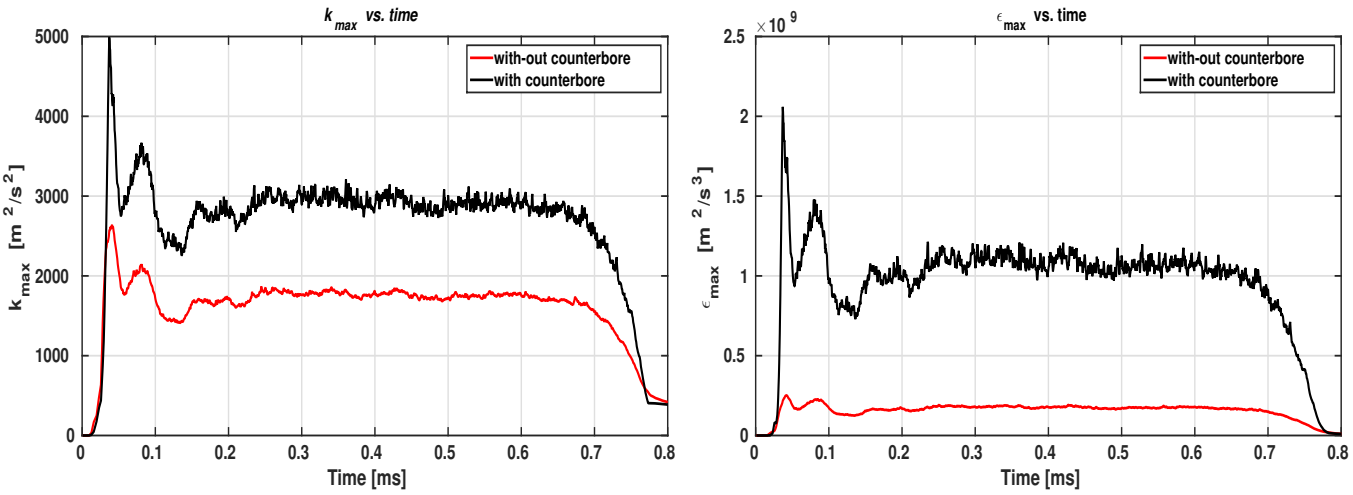

Figure 4.23: Max values of k and *epsilon* vs. time.

Clear differences between the two meshes were also apparent in the maximum values of turbulent kinetic energies and dissipation rates plotted in Figure 4.23 for both the meshes. It can therefore be said that it is important to resolve the counterbore region if a clearer picture of fuel-air mixing and turbulence is required.

Differential evaporation Of the three fuels, n-Pentane is the most volatile followed by iso-Octane and n-Undecane. For example, at 400K, the saturated vapor pressure of n-Pentane is 10.39 bar while those of iso-Octane and n-undecane are 2.08 bar and 0.13 bar, respectively.
The individual evaporation rates for the three components are shown in Figure 4.24 for the mesh with counterbore.

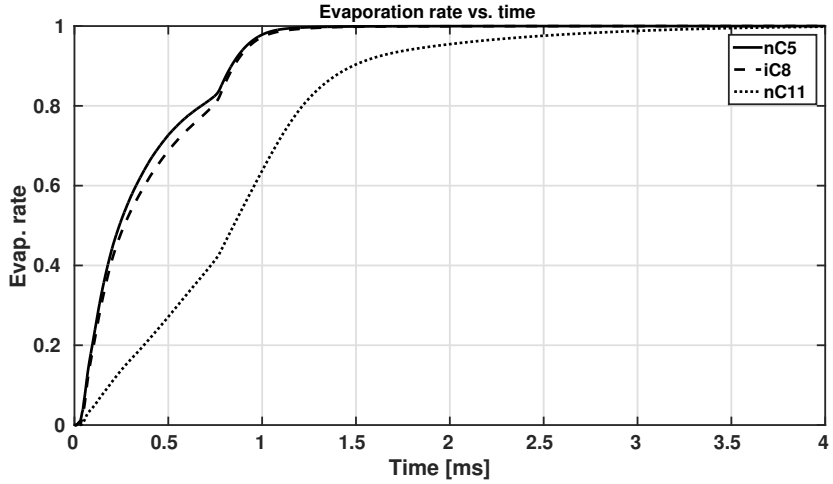

Figure 4.24: Individual evaporation rates for the three fuel components using the meshes with the counterbore.

The evaporation rates decrease in the same order as the volatility of the components: n-undecane evaporates much more slowly than iso-Octane and n-pentane. A contour plot of the vapor mass fraction for each component is shown in Figure 4.25 for the mesh without the counterbore.

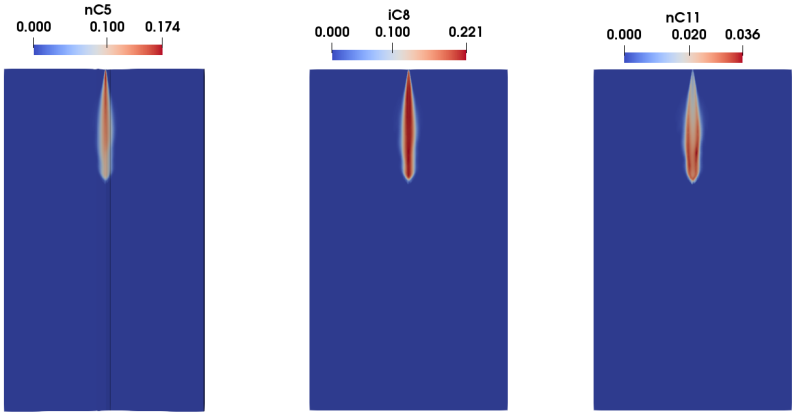

Figure 4.25: Contour plot of the individual vapor fractions predicted by the mesh with-out counterbore.

It is seen that that the vapor distribution is similar for iso-Octane and n-Pentane,

although the peak value is higher for isooctane as it has a higher content in the liquid mixture. It is seen that the least volatile component evaporates farther away from the injector. The trend is similar for the mesh with the counterbore (Figure 4.26) however, the peak value of vapor fractions is higher for the mesh with the counterbore.

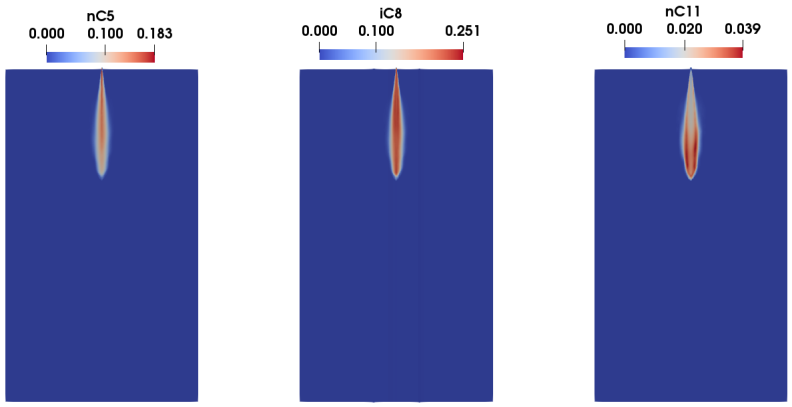

Figure 4.26: Contour plot of individual vapor fractions predicted by the mesh with counterbore.

To difference between the peak values of vapor fractions is seen clearer from the radial distribution of fuel vapor for the three components for both the meshes (see Figure 4.27).

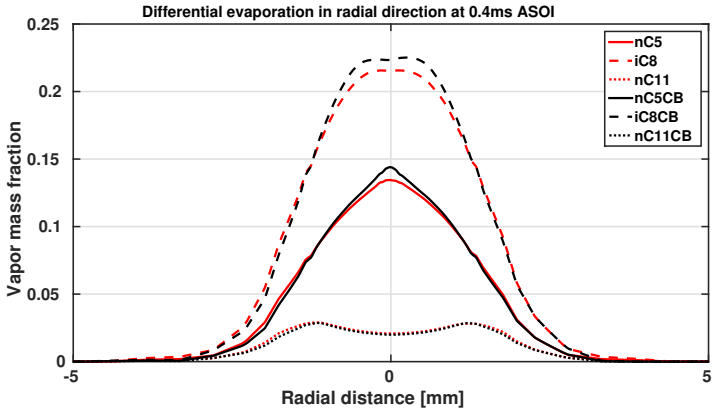

Figure 4.27: Differential evaporation in the radial direction at 0.4 ms ASOI, at z=15 mm, z-axis is the injector axis.

CB in the legend refers to counterbore. It is seen that the mesh with the counterbore predicts a higher peak vlaue of vapor fraction for n-Pentane and iso-Octane in and around the spray axis. This once again indicates that there is probably more mixing around the core region for the mesh with the counterbore. The difference in peak values is smaller for n-Undecane which evaporates in the periphery of the spray.

However, in both the meshes, a separate spatial preference can be seen for the evaporation of fuel components. It is seen that n-Undecane evaporates more around the periphery of the spray whereas the other two components evaporate around the

core of the spray. The probable reason for this distribution is that the more volatile components evaporates first in and around the spray axis. This would then bring the temperature of the core down and saturate it, and therefore the least volatile component n-Undecane, evaporates around the periphery of the spray.

Conclusion The following important conclusions can be drawn:

- Simulated liquid and vapor penetration for both the meshes showed reasonably good agreement with the experiment.
- A clear difference could be seen in mixing rate and turbulence values (for the fuel rich region) between the two meshes. The counterbore region of the resolved counterbore mesh, especially showed higher mixing rate and turbulence values. The results for the turbulence values can be seen in PaperIV.
- There was a noticeable difference in vapor distribution between the two meshes. The mesh with the counterbore predicted a higher peak vapor fraction for the fuel components.

It can therefore be said that if the interest is in overall spray behavior, especially the liquid and vapor penetrations and even the global evaporation rates, then the differences are small and it would suffice to have a mesh without resolving the counterbore. On the other hand if the interest is to look into the details of the spray like mixing rates and turbulence values then it has been shown that it is worthwhile to consider resolving the counterbore. It is also shown that resolving the counterbore makes a difference in the prediction of peak vapor distribution of the fuel components.

Chapter 5

Conclusion and outlook

As stated in Chapter 1 an important objective in this work was to create a solver for the coupled non-linear equations governing the evaporation of multicomponent fuels which should interface easily with the spray model and be able to handle increasing number of fuel components as required. This has been achieved using the SUNDIALS KINSOL solver. The solver was developed, implemented and tested for cases involving multicomponent fuels. The model was also validated with experimental data where applicable and has shown reasonably good agreement. The research questions raised in Chapter 1 have been answered here with important conclusions.

- What is the influence of considering non-ideal Vapor Liquid Equilibrium on the differential evaporation of multicomponent fuels?
  Non-ideal Vapor liquid equilibrium was seen to play an important role for multicomponent fuels with polar molecules (like alcohols). Simulations investigated a two component fuel comprising of Ethanol and iso-Octane injected in a constant volume spray chamber. The results from the study indicated that the assumption of ideal VLE based on Raoult's law does not accurately capture fuel spray behavior. The impact on liquid and vapor penetrations seems relatively small, but clear differences were revealed upon further analysis of spray structure. These observations also suggest that the influence of ethanol molecules on iso-octane is stronger than vice versa. This was especially because the difference in evaporation was clearly seen for E85 (85 % Ethanol by volume) case but not for the E10 case. For the E85 case, the radial fuel distribution for each of the component showed a clear difference between the ideal and non-ideal case. A higher fuel vapor mass fraction was seen for the non-ideal case for both the fuel components.

- What is the influence of resolving the injector orifice on spray predictions (diesel engine conditions) with respect to secondary breakup and evaporation of droplets and what is the influence on the predictions of turbulent kinetic energy and dissipation rate? How can a sufficient orifice resolution be justified?
  A grid sensitivity study was performed to quantify the uncertainty created by

the chosen fine mesh resolution for resolving the injector orifice and to justify the chosen resolution (9 cells resolving the orifice). Following that the simulations results were analyzed for the ECN spray A case. Resolving the mesh was seen to reduce the evaporation rate and increase the SMD, liquid and vapor penetration. Resolving the mesh was clearly seen to have a higher prediction of mixing rate and maximum turbulent kinetic energy and dissipation rate.

- In a Lagrangian parcel (or more specifically blob, as referred to in this work) having a size distribution of droplets, is it justifiable to assign the parcel velocity to all the size distributions? How does this assumption affect evaporation of the droplets under diesel engine conditions?

  A procedure was introduced to produced new child blob from the mass stripped of from parent blob. The new blob had it's own velocity. The influence of introducing new blobs was investigated for ECN spray A conditions. It was concluded that under high pressure and temperature diesel engine like operating conditions, the formation of new child blobs from stripped off mass, had no significant effect on spray predictions.

- What is the influence of resolving the counterbore of a GDI injector on spray formation with respect to evaporation of droplets and fuel-air mixing?

  The influence of resolving the counterbore on liquid, vapor penetrations and global evaporation rates is insignificant. However a clear difference could be seen in the details of the spray such as fuel-air mixing quantified by mixing rate and maximum turbulence values (k and ϵ) in the spray region. A recirculation zone could be seen in the counterbore. Mixing rate was seen to be higher for the mesh with the counterbore in the counterbore region and the fuel rich region. Maximum values of k and ϵ were seen to be higher for the mesh with the counterbore. Peak values of fuel vapor fraction were higher for the two most volatile components for the mesh with the counterbore.

In future the discrete multicomponent VSB2 spray model could be coupled to detailed chemical mechanisms and combustion models to study combustion of multicomponent fuels. It would be interesting to study how the difference in mixing rates, turbulence values and fuel vapor distributions between the resolved mesh and the unresolved mesh could influence the prediction of combustion of a multicomponent fuel. Having used a fine mesh for the resolved orifice case, in future it would be interesting to investigate LES of sprays to study finer spray structures.

It would also be interesting to couple the VSB2 to primary atomization models and obtain further insight into droplet breakup and evaporation. Currently the VSB2 model uses blob injection method which is computationally efficient but does not provide insight in to the primary breakup of droplets.

Bibliography

[1] Abani N., Kokjohn S., Park S., Bergin M., Munnannur A., Ning W., Sun Y., and Reitz R.D. "An improved spray model for reducing numerical parameter dependencies in diesel engine CFD simulations". In: *SAE Technical Paper* 2008-01-0970 (2008).

[2] Abraham, J. "What is adequate resolution in the numerical computations of transient jets?" In: *SAE paper* (1997).

[3] Abraham, J. and Magi, V. "A model for multicomponent droplet vaporization in sprays". In: *SAE Technical Paper* 980511 (1998).

[4] Allocca, L., Bartolucci, L., Cordiner, S., et al. "ECN Spray G Injector: Assessment of Numerical Modeling Accuracy". In: *SAE Technical Paper* 2018-01-0306 (2018).

[5] ASME. "Standard for Verification and Validation in Computational Fluid Dynamics and Heat Transfer, Reaffirmed 2016". In: (2009).

[6] Bader, A., Keller, P., and Hasse, C. "The influence of non-ideal vapor-liquid equilibrium on the evaporation of ethanol/iso-octane droplets". In: *International Journal of Heat and Mass Transfer 64* (2013), pp. 547–558.

[7] Baumgarten, C. *Mixture formation in internal combustion engines*. Springer, 2006.

[8] Computing at Lawrence Livermore National Laboratory. *SUNDIALS (SUite of Nonlinear and DIfferential/ALgebraic Equation Solvers)*. Accessed: 2020-03. 2020. URL: `https://computing.llnl.gov/projects/sundials/kinsol`.

[9] Crowe, C.T. *Multiphase flow handbook*. CRC press, 2006.

[10] Doué, N., Le Clercq, P., and Aigner, M. "Validation of a multicomponent-fuel droplet evaporation model based on continuous thermodynamics". In: *ICLASS* ICLASS06-250 (2006).

[11] Ducowicz, J.K. "A particle-fluid numerical model for liquid sprays". In: *Journal of Computational Physics* 35 (1980), pp. 229–253.

[12] ECN. *Diesel Data Search*. accessed: March 30, 2020. 2020. URL: `https://ecn.sandia.gov/ecn-data-search/`.

[13] ECN Spray G. *Sandia spray G Data*. accessed: June 30, 2020. 2020. URL: `https://ecn.sandia.gov/ecn-data-search/`.

[14] ECN7. *Topic 8*. accessed: 2020-09. 2020. URL: https://ecn.sandia.gov/ecn-workshop/ecn7-workshop/.

[15] El Wakil, M., Ueyhara, O., and Myers, F. "A theoretical investigation of heating-up period of injected fuel droplets vaporizing in air". In: *NACA Report No. TN 3179* (1954).

[16] F. Peng Karrhölm and N. Nordin. "Numerical investigation of mesh/turbulence/spray interaction for diesel applications". In: *SAE Technical Paper* 2005-01-2115 (2005).

[17] A. Fredenslund, L.R. Jones, and M. Prausnitz. "Group-contribution estimation of activity coefficients in nonideal liquid mixtures". In: *AIChe Jourbal* 21.6 (1975), pp. 1086–1099.

[18] Gosman, A.D. and Watkins, A.P. "Aspects of Computer Simulation of Liquid-Fueled Combustors". In: *Journal of Energy* **7** (1983), pp. 482–490.

[19] Gosman, A.D., and Watkins, A.P. *A computer prediction method for turbulent flow and heat transfer in piston/cylinder assemblies*. 1977.

[20] Hinrichs, J., Shastry, V., Junk, M. et al. "An experimental and computational study on multicomponent evaporation of diesel fuel droplets". In: *Fuel* 275 (2020). DOI: https://doi.org/10.1016/j.fuel.2020.117727.

[21] IEA Fuels and technologies. Accessed: 2020-10. 2019. URL: https://www.iea.org/fuels-and-technologies/renewables.

[22] IEA World energy outlook (Aviation). Accessed: 2020-10. 2019. URL: https://www.iea.org/reports/aviation.

[23] IEA World energy outlook (Data and staistics). Accessed: 2020-10. 2019. URL: https://www.iea.org/data-and-statistics/charts/co2-emissions-from-heavy-duty-vehicles-in-the-sustainable-development-scenario-2000-2030.

[24] IEA World energy outlook (International shipping). Accessed: 2020-10. 2019. URL: https://www.iea.org/reports/international-shipping.

[25] IEA World energy outlook (Tracking transport). Accessed: 2020-10. 2019. URL: https://www.iea.org/reports/tracking-transport-2020.

[26] Issa, R.I. "Solution of the implicitly discretized fluid flow equations by operator-splitting". In: *J. Comput. Phys.* 62 (1985), pp. 40–65.

[27] Jiao, Q., Ra, Y., and Reitz, R. "Modelling the influence of moelecular interactions on the vaporization of multi-component fuel sprays". In: *SAE Technical paper* 2011-01-0387 (2011).

[28] Jones, W.P., and Launder, B.E. "The Prediction of laminarization with a two-equation model of Turbulence". In: *International Journal of Heat and Mass Transfer* **15** (1972), pp. 301–314.

[29] Juric, D., and Tryggvason, G. "Computaions of boiling flows". In: *Int. J. Multiphase Flow Vol* **24** (1998), pp. 387–410.

[30] Karlsson, A. "Modeling auto-ignition, flame propagation and combustion in non-stationary turbulent sprays". PhD thesis. Göteborg: Department of Thermo and Fluid Dynamics, May 1995.

[31] Karlsson, A., Husberg, T., and Denbratt, I. "Analysis of advanced multiple injection strategies in a heavy-duty Diesel engine using optical measurements and CFD-simulations". In: *SAE paper* 2008-01-1328 (2008).

[32] Kawano, D., Senda, J., Wada, Y., Fujimoto, H. et al. "Numerical Simulation of Multicomponent Fuel Spray". In: *SAE Technical Paper* 2003-01-1838 (2003).

[33] Kawano, D., Tsukiji, K., Senda, J., Matsumura, E. et al. "Study on Multicomponent Fuel Spray with High Injection Pressure". In: *SAE Technical Paper* 2019-01-2282 (2019).

[34] Kazour, J., Befrui, B., Husted, H., Raney, M. et al. "Innovative sprays and particulate reduction with GDi injectors". In: *SAE technical paper* 2014-01-1441 (2014).

[35] Keller, P., Knorsch, T., Wensing, M., and Hasse, C. "Experimental and numerical analysis of iso-octane/ethanol sprays inder gasoline engine conditions". In: *International Journal of Heat and Mass Transfer 84* (2015), pp. 497–510.

[36] Kim, S., Yu, Y. and Ra, Y. "CFD Simulation of GDI Engine Cold Start Under Extreme Condition with Multi-Component Gasoline Fuels". In: *FISITA 2016 World Automotive Congress* F2016-ESYG-010 (2016).

[37] Knorsch, T., Heldmann, M., Zigan, L. et al. "On the role of physiochemical properties on evaporation behavior of DISI biofuel sprays". In: *Exp Fluids* 54.1522 (2013).

[38] Kösters, A., Karlsson, A. "Validation of the VSB2 spray model against spray A and spray H". In: *Atomization and Sprays* 26.8 (2016).

[39] Lippert, A.M. "Modeling of multicomponent fuels with application to sprays and simulation of diesel engine cold start". PhD thesis. University of Wisconsin-Madison, 1999.

[40] Lippert, A.M., and Reitz, R.D. "Modeling of Multicomponent Fuels Using Continuous Distributions with Application to Droplet Evaporation and Sprays". In: *SAE Technical Paper* 972882 (1997).

[41] Lucchini, T., D'Errico, G., Ettorre, D. "Numerical investigation of the spray-mesh-turbulence interactions for high-pressure, evaporating sprays at engine conditions". In: *International Journal of Heat and Flow* 32 (2011), pp. 285–297.

[42] Lupo. G., Ardekani, M.M., Brandt, L. et. al. "An Immersed Boundary Method for flows with evaporating droplets". In: *International Journal of Heat and Mass Transfer* 143.118563 (2019).

[43] Marchisio, D.L. and Fox, R.O. *Mutliphase reacting flows: Modelling and simulation*. Springer, 2007.

[44] National Standard Reference Data Series. Accessed: 2020-10. 2020. URL: `https://www.nist.gov/srd/national-standard-reference-data-series`.

[45] O'Rourke, P. "Statistical properties and numerical implementation of a model for droplet disperwsion in a turbulent gas". In: *Journal of Computational Physics* **83** (1989), pp. 345–360.

[46] Pati, A., Gierth, S., Haspel, P., Hasse, C. et al. "Strategies to Define Surrogate Fuels for the Description of the Multicomponent Evaporation Behavior of Hydrocarbon Fuels". In: *SAE Technical Paper* (2018). DOI: https://doi.org/10.4271/2018-01-1692.

[47] Payri, R., Morena, J.D.L, Monsalve-Serrano, J. et al. "Impact of counter-bore nozzle on the combustion process and exhaust emissions for light-duty diesel engine application". In: *International J of Engine Research* 20 (2019), pp. 46–57.

[48] Perini, F., and Reitz, R.D. "Improved atomization, collision and sub-grid scale momentum coupling models for transient vaporizing engine sprays". In: *International Journal of Multiphase Flow* **79** (2016), pp. 107–123.

[49] Pilch, M., Erdman, C.A. "Use of breakup time data and velocity history data to predictthe maximum size of stable fragments for acceleration-induced breakup of a liquid drop". In: *International Journal of Multiphase Flow* vol. 13 (1987), pp. 741–757.

[50] Qubeissi, M., Al-Esawi., Sazhin, S. et. al. "Ethanol/Gasoline Droplet Heating and Evaporation: Effects of Fuel Blends and Ambient Conditions". In: *Energy & Fuels* 32 (2018), pp. 6498–6506. DOI: {10.1021/acs.energyfuels.8b00366}.

[51] Qubeissi, M., Sazhin, S.S., and Elwardany, A.E. "Modelling of blended Diesel and biodiesel fuel droplet heating and evaporation". In: *Fuel* 187 (2017), pp. 349–355.

[52] Ra, Y., and Reitz, R.D. "A vaporization model for discrete multi-component fuel sprays". In: *International Journal of Multiphase Flow* **35** (2009), pp. 101–117.

[53] Ranz, W.E. and Marshall, W.R. *Internal Combustion Engine Modelling.* Hemisphere Publishing, 1952.

[54] Reitz, R.D. "Modeling Atomization Processes in High-Pressure Vaporizing Sprays". In: *Atomization and spray technology 3* (1987), pp. 309–337.

[55] Reitz, R.D., and Diwakar, R. "Structure of High-Pressure Fuel Sprays". In: *SAE-paper* 870598 (1987).

[56] Ren, Z., Zhang, L. and Ren, X. "A hybrid multicomponent model for the vaporisation simulation of gasoline drop". In: *Combustion Theory and Modelling* 23:2 (2019), pp. 210–225.

[57] Renksizbulut, M., and Yuen, M.C. "Numerical study of droplet evaporation in a high-temperature stream(Article)". In: *Journal of Heat Transfer* 105 (1983), pp. 389–397.

[58] Henri Renon and J M Prausnitz. "Local Compositions in Thermodynamic Excess Functions for Liquid Mixtures". In: *AIChE* 14.1 (1968), pp. 135–144.

[59] Richardson, L.F. "The approximate arithmetical solution by finite differences of physical problems involving differential equations, with an application to the stresses in a mansory dam". In: *Transactions of the royal society of London, Ser. A* **210** (1910), pp. 307–357.

[60] Saha, k., Som, S. et al. "Modeling of internal and near-nozzle flow for a GDI fuel injector". In: *Proceedings of the ASME 2015 Internal Combustion Engine Division Fall Technical Conference* (2015).

[61] Schlottke, J., Weigand, B. "Direct numerical simulation of evaporating droplets". In: *Direct numerical simulation of evaporating droplets* 227 (2008), pp. 5215–5237.

[62] Schmehl, R., Maier, G., and Wittig, S. "CFD Analysis of Fuel Atomization, Secondary Droplet Breakup and Spray Dispersion in the Premix Duct of a LPP Combustor". In: *Eight Int. Conf. on Liquid Atomization and Spray Systems, Pasadena, CA, USA* (2000).

[63] Senecal P.K., Pomraning E., Richards K.J., and Som S. "Grid-Convergent Spray Models for Internal Combustion Engine Computational Fluid Dynamics Simulations". In: *Journal of Energy Resources Technology* **136**.JERT-13-1108 (2014).

[64] Tamim J., and Hallett W.L.H. "A Continuous thermodynamic model for multicomponent droplet vaporization". In: *Chem Eng Sci* 50.18 (1995), pp. 2933–2942.

[65] The OpenFOAM Foundation. *OpenFOAM 2.2.0*. Accessed: 2020-10. 2013. URL: `https://openfoam.org/version/2-2-0/`.

[66] Tu, P., Xu, H et al. "Numerical Investigation of GDI Injector Nozzle Geometry on Spray Characteristics". In: *SAE technical paper* ICEF2015-1112 (2015).

[67] Verein Deutscher Ingenieure. *VDI-Wärmeatlas*. Springer, 2006.

[68] Wagh, M., Joo, N., Zoldak, P., Won, H. et al. "Real Fuel Modeling for Gasoline Compression Ignition Engine". In: *SAE Technical Paper* 2020-01-0784 (2020).

[69] Wang, Y., Ge. H., and Reitz, R. "Validation of Mesh and Timestep-Independent spray Models for Multi-Dimensional Engine CFD simulation". In: *SAE Int. J. Fuels Lubr* **3** (2010), pp. 277–302.

[70] Weller, H. G et al. "A tensorial approach to computational continuum mechanics using object-oriented techniques". In: *Computers in Physics* **12** (1998), pp. 620–631.

[71] Chao-Cheng Wen and Chein-Hsiun Tu. "Vapor–liquid equilibria for binary and ternary mixtures of ethanol, 2-butanone, and 2,2,4-trimethylpentane at 101.3kPa". In: *Fluid Phase Equilibria* 258.2 (2007), pp. 131–139. ISSN: 03783812. DOI: `10.1016/j.fluid.2007.06.005`.

[72] Yang, S., Ra, Y., Reitz, R.D., Wege, B.V.D., and Yi, J. "Development of a realistic multicomopnent fuel evaporation model". In: *Atomization and Sprays* (2010).

[73] Zhang, L. and Kong, S-C. "High Pressure Vaporization of Multi-component Petroleum-biofuel mixtures under Engine Conditions". In: *Combustion and Flame* 158 (2011), pp. 1705–1717.

[74] Zhang, L. and Kong, S-C. "Modeling of multi-component fuel vaporization and combustion for gasoline and diesel spray". In: *Chemical Engineering Science* 64 (2009), pp. 3688–3696.

[75] Zheng, L., Ma, X., Wang, Z., and Wang, J. "An Optical Study on Liquid-Phase penetration, Flame Lift-Off Location and Soot Volume Fraction Distribution of Gasoline-Diesel Blends in a Constant Volume Vessel". In: *Fuel* 139 (2014), pp. 365–373.